Mechanism of Formation of Late Miocene Cauldrons in the Southern District of Northeast Japan

Hiroaki KOMURO

(Received September 5, 1987)

Two upper Miocene cauldrons which differ from other conventional type cauldrons were found in the Aizu district, Fukushima Prefecture, Northeast Japan. They are characterized by polygonal outlines with diameters of ca. 5 km, eruption after caldera collapse, and preceding domal rises. The domal rise was caused by the ascent of a magma reservoir and was 15–25 km in diameter with a height of 400 m over. The caldera floor subsided 150–200 m in depth.

Two-dimensional finite element analyses (FEM) simulated the doming and its stress pattern. The earth's crust was assumed to undergo elasto-plastic deformation . The resuslts of the analyses are as follows:

1. The diameter of the surface dome does not change through the rising of the dome. Horizontal tensile stresses concentrate around the dome apex.

2. The diameter of the surface dome is sensitively controlled by the depth of the reservoir.

3. The reservoir which causes the dome with a diameter of about 20 km is situated less than ca. 8 km in depth.

4. When two reservoirs simultaneously ascend in less distance, the surface cauldrons merge into one.

Scale model experiments of a reduced scale of 1/100,000 were carried out in order to simulate the formation process of the cauldron. The model earth's crust was made of powdered clay and sand. The ascending magma reservoir was imitated by a hardened putty ball moved by a motor, and the evacuation of magma was simulated by the evaporation of dry ice. The results of the experiments are as follows:

1, Radial and concentric fractures were formed around the dome apex, and a small block surrounded by these fractures was subsided. Continuous ring fractures did not developed. Consequently, a caldera which showed an irregular polygonal shape with diameter of 2–3 cm was formed. The displacements of the boundary fauslts were 1–2 mm when the uplift of the dome reached 7 mm.

2. When the material cohesion was higher, concentric fractures did not developed.

3. The subsurface cavity caused by the evaporation of dry ice produced outward dipping ring fractures and a circular cauldron. These fractures developed upward from the subsurface cavity. No radial fractures were formed.

These analyses and experiments suggest the following points. Subsidence of the polygonal cauldron is accommodated with the horizontal extension on the dome apex. The fracturing of the polygonal cauldron develops from the earth's surface to the magma reservoir by doming, so that eruption begins after these fracturing and surface collapse. However, the circular cauldron and ring fractures are formed after the large evacuation of magma. If the cohesion of the crust is higher, the ring fracture eruption and the subsidence of the circular cauldron may follow central vent or radial fracture eruption.

CONTENTS

I. INTRODUCTION

Most of cauldrons, e.g. collapse calderas, Glencoe type cauldrons, *etc.*, have been believed to be more or less circular or cirquelike in shape except volcano-tectonic depressions (WILLIAMS, 1941).   A large magma reservoir has been assumed under the cauldron though its size and depth remained uncertain.   A central block of the cauldron has been considered to have subsided into the magma reservoir along ring fractures (SMITH and BAILEY, 1968).   Evacuation of magma or density inversion of magma to the roof of the reservoir has been regarded as a trigger of subsidence (CLOUGH *et al.,* 1909; WILLIAMS, 1941).

These conventional concepts are critically discussed in this paper on the basis of field evidence and experimental results.   The author's interest in this problem is mainly devoted to the fracturing and subsidence of cauldrons.

Some of the Glencoe type cauldrons and ring complexes show circular or elliptic outlines, and ring fractures are observed around these cauldrons (CLOUGH *et al.,* 1909; RICHEY, 1961).   However, OIDE (1968) showed that the outline of some Krakatoan calderas in Japan is not circular but polygonal.   Ring fractures are not confirmed in most Krakatoan calderas.

In recent years, the presence of magma reservoirs has been confirmed under some calderas, e.g. Yellowstone caldera, Kilauea caldera, *etc.* (EATON *et al.,* 1975; KOYANAGI and ENDO, 1976; SANDERS, 1984).   As a most plausible mechanism for the formation of cauldrons, collapse of the roof of reservoir into the underlying magma body has been suggested.   Two main causes of the collapse are proposed: density difference between the roof rock and the magma (CLOUGH *et al.,* 1909), and evisceration of the magma reservoir associated with the climactic eruption from central vents (WILLIAMS, 1941) or ring fractures (SMITH and BAILEY, 1968).   Both hypotheses assume that the volume of the caldera collapse is balanced with that of ejected magma.

On the other hand, FUJITA (1967) insisted that most of Miocene cauldrons in Japan was collapsed before the eruptions. He concluded that these cauldrons are characterized by polygonal outline, and that the caldera collapse was not caused by evisceration of magma reservoirs but by local doming. The model of this type cauldron was established in the Motojuku region of the central Japan (FUJITA *et al.*, 1970).

The author reconsiders these cauldron problems on the basis of field evidence and simulations. The present paper falls into the following three main parts.

First, field evidence of the polygonal cauldron is described on the basis of the author's survey of two late Miocene cauldrons in the Aizu district, southern part of Northeast Japan (Chapter II–IV). Since these cauldrons are not covered by thick ejecta or sediments and have not been destroyed by erosion, their structures can be easily revealed.

Second, numerical and experimental analyses on the formation mechanism of the cauldrons are described (Chapter V). The position of the magma reservoir associated with cauldron structure was eastimated by means of plastic analyses. These analyses were carried out by finite element method (FEM). Faulting mechanism was analyzed by scale model experiments composed of brittle material (mixture of powdered clay and sand). These experimental results demonstrated the order of formation of radial and concentric fractures and the formation mechanism of ring fractures. Previous experiments on the formation of grabens and salt dome tectonics (CLOOS, 1939; PARKER and McDOWELL, 1955; CURRIE, 1956; *etc.*) are also discussed in connection with the formation mechanism of the cauldrons.

Third, apart from this field, generalized consideration on cauldron formation is given. Although these numerical and experimental works were carried out in order to simulate the cauldrons in this field, these results may be applied to other type cauldrons, e.g. collapse calderas, ring complexes and Glencoe type cauldrons, *etc.* (Chap. VI)

Terminology

According to WILLIAMS (1941), "calderas are large volcanic depressions, more or less circular or cirquelike in form, the diameters of which are many times greater than those of the included vent or vents, no matter what the steepness of the walls or form of the floor". WILLIAMS and McBIRNEY (1979) noted, "there is no sharp demarcation between calderas and cauldrons...", and "the principle difference is that calderas are associated with collapse following a withdrawal of magma. While cauldrons are thought to result from a passive foundering of the roof of a static or rising body of magma". Karakatoan type calderas are "formed by the foundering of the tops of large composite volcanoes following explosive eruptions of siliceous pumice". Volcano-tectonic depressions were discriminated from calderas and cauldrons, because they are bounded by faults of tectonic origin.

SMITH and BAILEY (1968) accepted WILLIAMS' definition of calderas, but they used the term cauldron "to include all volcanic subsidence structures regardless of shape of

size, depth or erosion, or connection with surface volcanism". Therefore, the term cauldron is the most general concept of volcanic subsidence including cauldron subsidence, collapse caldera, volcano-tectonic depression and others. The term cauldron is used according to SMITH and BAILEY (1968) in this paper.

The term 'cauldron subsidence' means a more restrictive concept. It is used to be "a structure resulting from the lowering along a steep ring fracture of a cylindrical block into a magma chamber" (after Glossary of Geology, 2nd ed.). On the other hand, according to YOKOYAMA (1969, 1974), Krakatoan calderas of WILLIAMS (1941) may not always be formed as a result of withdrawal of magmatic support. Accordingly, the term caldera should be used as morphological feature regardless of its genetic significance.

FUJITA (1976) and FUJITA et al. (1970) revealed that the Green Tuff movement in Japan is characterized by the formation of cauldrons which were formed in relation to acidic to intermediate volcanism. This type of cauldron is characterized by (1) a polygonal cauldron with the development of normal to vertical faults at the apex of the domal rise, (2) caldera collapse occurred before the main eruption, and (3) secondary collapse nested in the primary polygonal cauldron after the voluminous outpouring of lavas.

Although FUJITA et al. (1970) called this type cauldron a 'depression basin', it is better to use the term cauldron for such volcanic collapse structure. Then, the term 'Motojuku type cauldron' is employed here, which refers to the formation process and the structure of the volcanic collapse basin typically shown in the Motojuku cauldron.

II. GEOLOGY

Most of cauldrons are more or less cirquelike in shape, and their central blocks have been considered to have subsided into the magma reservoir along ring fractures. However, FUJITA (1967) insisted that Miocene cauldrons formed during the Green Tuff movement in Japan show polygonal outlines and the their fractures consist of mutually intersecting normal faults. OIDE (1968) also pointed out that some Quaternary Krakatoan calderas in Japan show polygonal outlines. Accordingly, the outline of cauldron and fracture system must be critically studied in field.

The order of occurrence between eruption and caldera collapse should receive much attention. The caldera collapse has been believed to occur generally after large eruptions. However, FUJITA (1967) pointed out that some cauldrons were collapsed before the main eruption.

Special attention should be also given to the vertical movements associated with cauldron formation. Although SMITH and BAILEY (1968) concluded that the regional tumescence emerged before the formation of Valles Caldera, they did not give the evidence of the tumescence but ring fractures. FUJITA et al. (1974) suggested that local doming occurred before cauldron formation on the basis of the stratigraphic analyses.

In order to study these cauldron problems more critically, Quaternary calderas may be inadequate, because they are usually covered by thick ejecta. On the contrary, the Paleogene to Neogene cauldrons in Japan may be suitable for the study of the cauldron structure because of their appropriate erosion levels. Especially, in the Green Tuff region of Northeast Japan, many Miocene cauldrons are known. Therefore, this region is one of the best fields to study the cauldron problems. The author studied two upper Miocene cauldrons in the Aizu district, Fukushima Prefecture, the southern part of Northeast Japan.

The surveyed area is shown in Fig. 1. This area is located in the 'Tsugawa-Aizu province' (SHIMAZU, 1973) of the Green Tuff region. This province is characterized by NW–SE tectonic trend, voluminous felsic volcanism, *etc.*
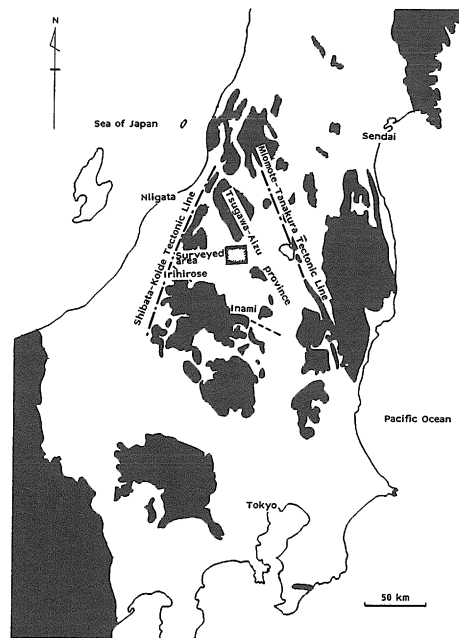
Fig. 1. Location of the surveyed area in the southern part of Northeast Japan. Black painted areas show the pre-Tertiary rocks.

Two late Miocene cauldrons, the Sunagohara and Honna cauldrons, which show not circular but polygonal outlines of ca. 5 km in diameter, were found in this area (Fig. 2). The Miocene Series in this area can be divided into the following formations in ascending order; the Takisawagawa, Ōtani, Iriyamazawa, Urushikubo, Shiotsubo, and Sunagohara Formations. The Fujitōge and Ōbetōge Formations range in age from the latest Miocene to Pliocene, and the Komadotōge Formation is assigned to the Pliocene (Fig. 2, 3, 4, 5; Table 1). Two Quaternary volcanoes, Numazawa and Hakaseyama

Volcanoes, are arranged in a direction of NW–SE.

Rhyolitic and dacitic volcanic activity was predominant throughout Miocene time. Minor basaltic volcanism occurred in the middle to late Miocene mainly in the western area, and andesitic rocks occurred only in the eastern area.

The regional stress field in Northeast Japan was considered to have abruptly changed after the Miocene (NAKAMURA, 1969; TAKEUCHI, 1981), i.e. from horizontal E–W tensile stress during the Miocene to horizontal E–W compression at the beginning of the Pliocene. However, according to recent works on the regional stress field (SATO et al., 1982; SATO, 1986), the horizontal stress pattern was almost neutral from the middle Miocene to early Pliocene (15–5 Ma).

The outlines of the late Miocene cauldrons in this field are not elongated in one direction, though the main tectonic trend of this field is NW–SE. This suggests that the formation of the cauldrons was not controlled by the deviatoric regional stress field. This is also concordant with the Sato's conclusion that the stress field was not deflected but neutral during the late Miocene. The cauldron formation was possibly influenced only by the ascending magma reservoir, being free from the regional horizontal tension or compression.

II–1.   Description of Geology

The outline of the geology relating to the late Miocene cauldrons and their basement rocks are described below.

II–1–1.   Takisawagawa Formation

The Takisawagawa Formation was named by HIRABAYASHI (1966) and was re-defined by SHIMADA and IZAWA (1969). This formation corresponds to the Tamanashi Formation of KITAMURA et al. (1968).

Type locality: Takisawagawa, Kanayama-chō, Ōnuma-gun, Fukushima Prefecture.

Stratigraphic relation: This formation unconformably covers the pre-Tertiary rocks, but the relation is not observed in this area.

Thickness: 1000 m+.

Lithofacies: This formation is composed of rhyolite lavas, rhyolitic tuff breccias and fine tuffs. The lowermost member crops out around the Kirikitazawa and Kasagi-zawa rivers. The lower member consists of rhythmic alternated fine tuffs, and the upper member consists of rhyolite lavas and tuff breccias (SHIMADA and IZAWA, 1969). SHIMADA and UEDA (1979) dated the rhyolite to be 23 Ma by K-Ar method.

II–1–2.   Ōtani Formation

This formation is assumed to correspond to the Ōshio Formation in the western Aizu region (SHIMADA and IZAWA, 1969). However, the author gives a new name to the formation which is distributed in the surveyed area, because both formations do not continue each other. They are subdivided into the Miyashita Mudstone Member (the

E

Kotsubaki

Yanaizu
Tokorozawa

Nishikata

Takiya

Ōmine

Miyashita

Ōtani

Yunotake

River Tadami

Hayato

A   B

Lake Numazawa

Kawaguchi

Sunagohara

D

Numazawa
Volcano

Honna

Ōtani-touge
Pass

Kabuchū

Asamata
Iriyamazawa

Tamanashi

Ōnarisawa

Takamori

Ōbetouge

Hakaseyama
Volcano

Shimo-nakatsugawa

C

N

0 1 2 3 4 5 km

1
2
3
4
5
6   a   b
7
8
9   a   b   c   d
10   a   b
11
12
13   a   b
14   a   b   c   d
15   0~5°   ~10°   ~30°   ~60°   ~90°

Fig. 2. Geologic map of the Miyashita district, Fukushima Prefecture.

1: Quaternary volcanoes, 2: terrace deposits, 3: Komadotōge Formation, 4: Fujitōge Formation, 5: Shiotsubo Formation, 6: Sunagohara Formation (a: volcaniclastic rocks, b: perlite), 7: Honna Formation, 8: Obetōge Formation, 9: Urushikubo Formation (a: volcaniclastic rocks, b: andesitic lavas and pyroclastic rocks, c: rhyolite, d: mudsone), 10: Iriyamazawa Fomation (a: pumice tuff, b: basaltic lapilli tuff), 11–12: Otani Formation (11: Nishikata Tuff Member, 12: Miyashita Mudstone Member), 13: Takisawagawa Formation (a: volcaniclastic rocks, b: rhyolite), 14: dikes (a: rhyolite, b: dacite, c: andesite, d: basalt), 15: dip and strike.

Compiled from HAYAKAWA *et al.* (1968) and SHIMADA and IZAWA (1969) (especially on the Takisawagawa Formation), SUZUKI *et al.* (1968) (the area to the north of Nishikata) and KOMURO (1978, 1984).
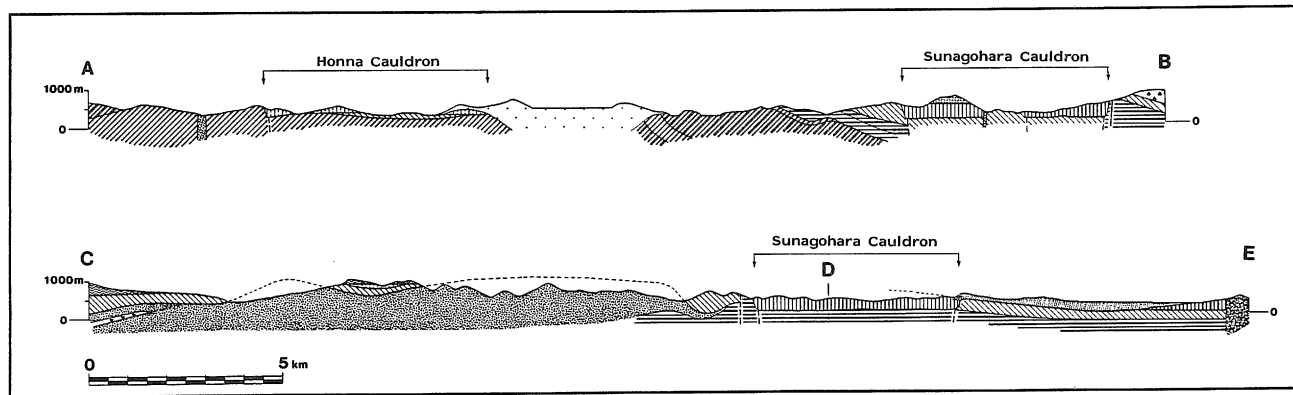
Fig. 3.   Geologic sections.   Locations of the sections and legend are shown in Fig. 2–2.
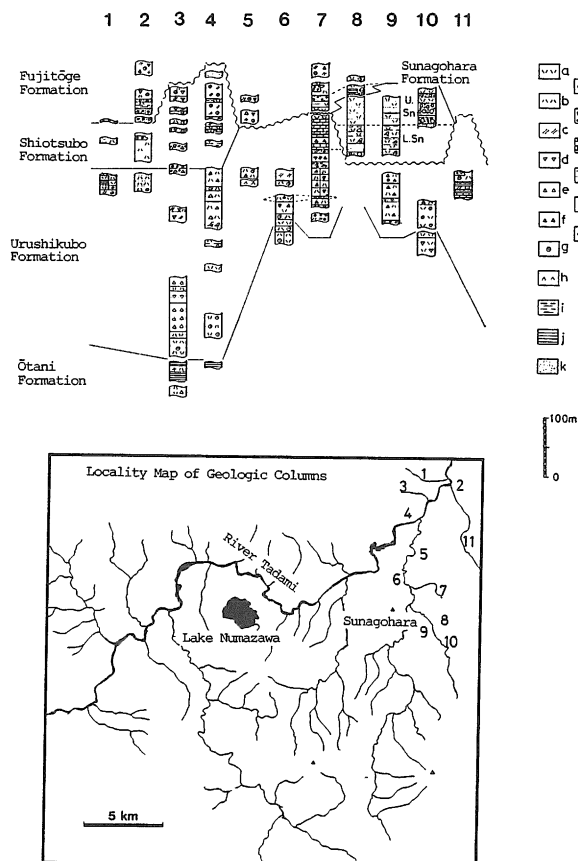
Fig. 4. Geologic columns in the northeast part of the Miyashita district, Fukushima Prefecture.

a: very fine tuff, b: fine tuff, c: coarse tuff, d: felsic lapilli tuff, e: felsic tuff breccia, f: andesitic tuff breccia, g: pumice, h: rhyolite lava, i: siltstone, j: mudstone, k: sandstone, l: conglomerate, m: sedimentary breccia, n: calcareous sandstone, o: lamination, p: alternated beds, q: slump bedding.

lower member) and the Nishikata Tuff Member (the upper member).

II-2-2-(a)   Miyashita Mudstone Member

This member was named by Kitamura et al. (1968).

Type locality: Miyashita, Mishima-chō, Ōnuma-gun, Fukushima Prefecture.

Stratigraphic relation: Conformable relation with the Takisawagawa Formation.

Thickness: 300 to 350 m.

Lithofacies: This member consists of black mudstone to sandy mudstone. It shows clear bedding and yields *Globigerinoides bisphericus* and others (Kitamura et al., 1968).

Table 1. Correlation table of the Aizu district.
Compiled from SHIMADA and IZAWA (1969), SHIMA-
DA et al. (1974), SUZUKI et al. (1972), and KOMURO
(1984).

Age		Tadami, Kobayashi	Miyashita	Aizu Basin	
Holocene			Numazawa Volcano		
Pleistocene			Hakase-Yama Volcano	Nanaorizaka F.	Senaka-Aburiyama F.
Pliocene		Komado-tōge F.		Izumi F.	
		Ōbetōge F.	Honna F. / Sunagohara F.	Fujitōge F.	
Miocene	Late	Yashioda F. / Matsuzakatōge F.		Shiotsubo F.	
		Fuzawa F.	Urushikubo F.	Urushikubo F.	Hongō F.
	Middle	Ogawazawa F.	Iriyamazawa F.	Ogino F.	
		Ōtani F. / Ōshio F.	Nishikata Tuff Member / Miyashita Mudstone Member	Tanaka F.	
		Takisawagawa F.		Kannon F.	

II-1-2-(b) Nishikata Tuff Member

This member was named by KITAMURA et al. (1968), but it was regarded as a formation unit. The author considers it to be a member unit because of the interfingering relation between the Miyashita and Nishikata Members.

Type locality: Nishikata, Mishima-chō, Ōnuma-gun, Fukushima Prefecture.

Stratigraphic relation: This member conformably overlies the Miyashita Mudstone Member around Miyashita, but directly covers the Takisawagawa Formation in the northern area because the mudstone member pinches out northward.

Thickness: 50–300 m.

Lithofacies: This member consists of greenish tuff breccia, pumice tuff and lapilli tuff. *Serripes* cf. *makiyamai* and *Delectopecten peckhami* were obtained (HAYAKAWA et al., 1968).

II-1-3. Urushikubo Formation

This formation was named by SUZUKI (1951).

Type locality: Urushikubo, Takasato-mura, Yama-gun, Fukushima Prefecture.
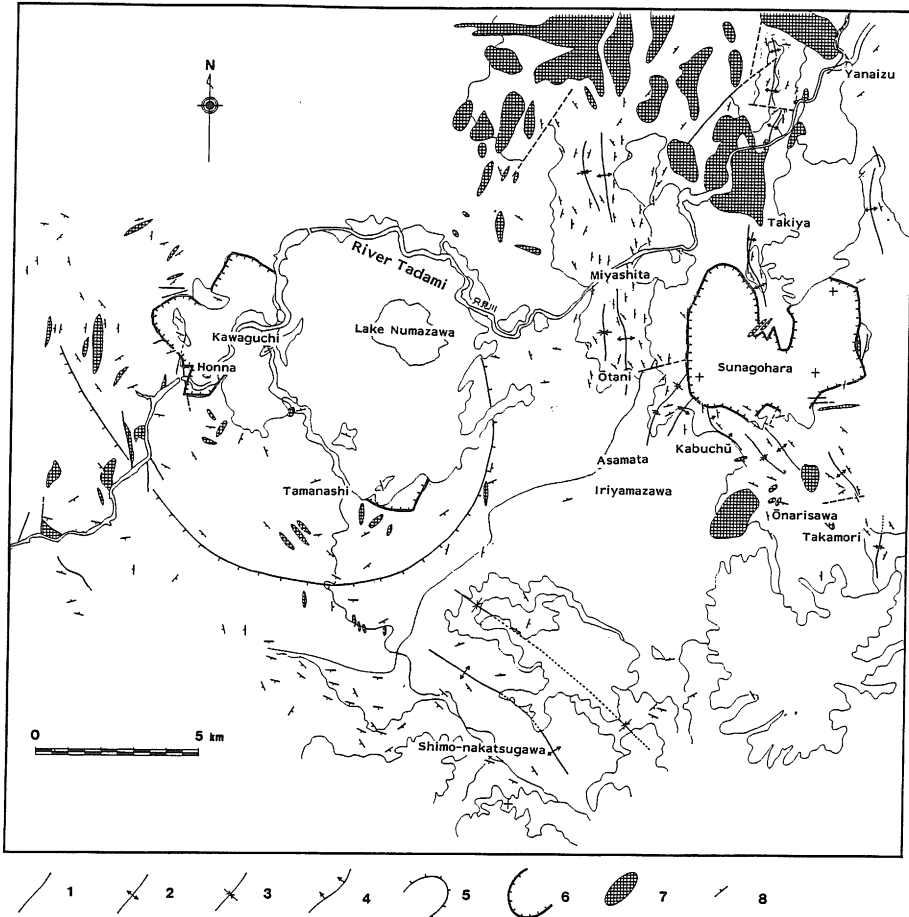
Fig. 5.   Structural map of the Miyashita district, Fukushima Prefecture.
1: fault, 2: anticlinal axis, 3: synclinal axis, 4: flexure, 5: dome structure, 6: cauldron structure,
7: dike, 8: dip and strike.

Stratigraphic relation: This formation conformably overlies the Iriyamazawa
Formation, but unconformably covers the Ōtani Formation near Takamori and from
Miyashita to Ōtani.

Thickness: 250–400 m.

Lithofacies: The main part of this formation consists of rhyolite lava, fine tuff,
perlitic tuff breccia, tuffaceous sandstone, mudstone, calcareous sandstone and con-
glomerate.

The lower member consists of conglomerates and alternating beds of laminated fine
tuff and tuffaceous siltstone.   Thin calcareous sandstone beds are rarely intercalated.

In the eastern area, andesitic lavas and pyroclastic rocks occur, which were named

the Myōjingatake andesitic member (SUZUKI and YOSHIDA, 1956). The andesitic member is not contained in the Ōtani Formation in this area, though Suzuki *et al.* (1972) mentioned that this member corresponds to the Ogino (Ōtani) and Urushikubo Formations. This member has been dated as 8.8±0.4 Ma (K-Ar) (New Energy Foundation, 1984).

Chlamys kaneharai (YOKOYAMA), *Placopecten akihoensis* (MATSUMOTO), *Terebratalia tenuis* (HAYASAKA), *Coptothyris adamusi* (DAVIDSON) and *Miyagipecten matsumoriensis* MASUDA were reported from this formation (SUZUKI and YOSHIDA, 1956). HAYAKAWA *et al.* (1972) described the foraminiferal assemblage ranging from N. 9 to N. 10, while SUZUKI (1986) reported the assemblage N. 10–N. 12 in the Aizu Basin region.

II-1-4. Shiotsubo Formation

This formation was named by SUZUKI (1951).

*Type locality*: Shiotsubo, Takasato-mura, Yama-gun, Fukushima Prefecture.

Stratigraphic relation: This formation conformably overlies the Urushikubo Formation.

Thickness: 150 m.

Lithofacies: This formation consists of pumice tuffs, well-stratified acidic fine tuffs and medium sandstones. Well-rounded pebbles are contained in the pumice tuff, and pebble conglomerate beds are intercalated at the base of this formation near Yanaizu and Tokorozawa.

Serripes yokoyamai (OTSUKA), *S. laperousi* (DESHAYES), *Tellina protovenulosa* NOMURA, and *Chlamys* cf. *kaneharai* (YOK.) were reported from the medium sandstone (SUZUKI and YOSHIDA, 1956). In the Aizu basin region, this formation yields the Yama fauna (OTSUKA, 1941).

II-1-5. Sunagohara Formation

This formation was named by HAYAKAWA *et al.* (1968) and corresponds to the lower Onogawara Formation of KITAMURA *et al.* (1968).

Type locality: Sunagohara, Yanaizu-chō, Kawanuma-gun, Fukushima Prefecture.

Stratigraphic relation: This formation unconformably covers the Urushikubo and Ōtani Formations. The main part of the unconformity surface steeply dips to the inside of the sedimentary basin. This formation lies almost horizontally and abuts on the unconformity surface. The abutting beds of this formation amount to about 150 m thick. The upper member of this formation partly covers the gently dipping unconformity surface.

Thickness: 400 m.

Lithofacies: This formation consists of marginal sedimentary breccias, fine tuffs and perlite lavas (Figs. 6, 7).

The marginal breccias, which become coarser toward the margin, are not stratified and poorly sorted. They contain numerous angular rock fragments of 3–4 m in
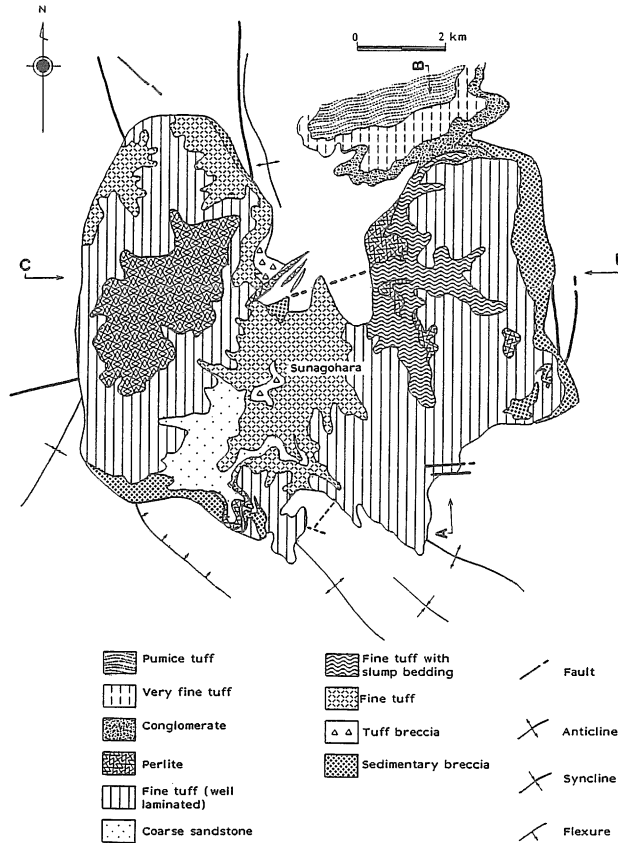
Fig. 6.   Lithofacies of the Sunagohara Formation and structures of the basement.
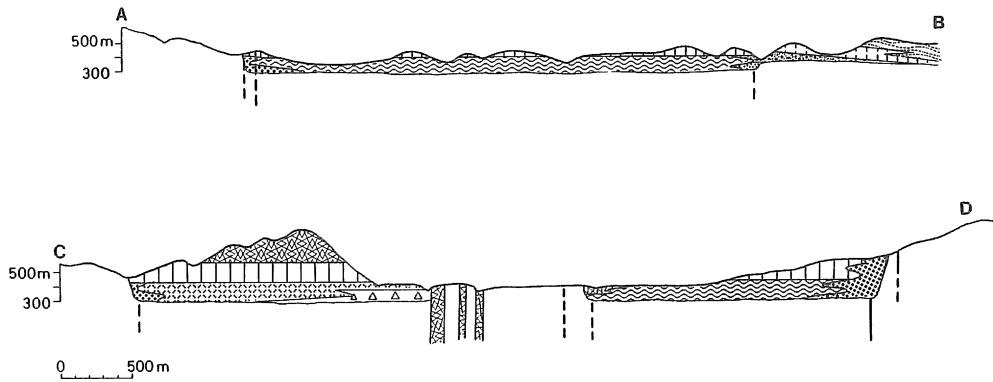

Fig. 7.   Geologic sections of the Sunagohara cauldron.   Location and legend are shown in Fig. 6.

maximum diameter. These fragments of the east margin consist mostly of andesite blocks derived from the Myōjingatake andesitic member, while those of the southern margin consist mainly of blocks of fine tuff and lapilli tuff derived from the Urushikubo Formation. Matrix of the breccias is the same material as these blocks, and rounded granules and pebbles are scarcely contained. Accordingly, these marginal breccias are regarded as sedimentary breccia of talus origin. These breccias interfinger with the lower to upper members of this formation. Since mega-blocks are not included, the breccias may be assigned to mesobreccias of LIPMAN (1976).

The lowermost part is composed of alternating beds of perlitic tuff breccias and tuffaceous sandstones.

The lower member consists of fine tuff, which is partly suffered kaolinitization. In the eastern area, they are disturbed by slumping. Coarese sandstone beds are intercalated in the southern area.

The upper member consists of non-altered fine to very fine tuff with remarkable lamination, indicating the lithofacies of lake deposit origin. This member lies almost horizontal.

Most of the perlite lavas overlie the upper member, but some lavas are intercalated in the lower member. Phenocrysts of quartz, plagioclase, biotite and hornblende are embedded in black glass with perlitic structure. The radiometric ages of the lavas range from 0.21 Ma (K-Ar) to 1.23 Ma (FT) (New Energy Foundation, 1984).

Perlite dikes are found near the margin of this formation. They strike NE–SW along the margin, and cut the Sunagohara Formation and the basements.

Cryptomeria japonica (LINN. fil.) D. DON and *Populus maximowiczii* A. HENRY, and some pollen remains were reported (SUZUKI, 1986).

II–1–6. Honna Formation

This formation was named by SHIMADA and IZAWA (1969).

Type locality: Honna, Kanayama-chō, Ōnuma-gun, Fukushima Prefecture.

Stratigraphic relation: This formation unconformably covers the Urushikubo and Takisawagawa Formations. The unconformity surface abruptly dips to the basin along the northern and the western margins, where sedimentary breccias are distributed.

Thickness: 200 m.

Lithofacies: The main part of this formation is composed of dacitic tuff breccia which is slightly altered. Marginal sedimentary breccias consist of fragments of rhyolite and tuff with 2–3 m in maximum diameter which were derived from the nearby Takisawagawa Formation (Fig. 8). The matrix of the breccia also consists of the same material. These breccias are also of talus origin.

II–1–7. Fujitōge Formation

This formation was named by SUZUKI (1951). In this area, the lower and middle members of this formation are distributed.
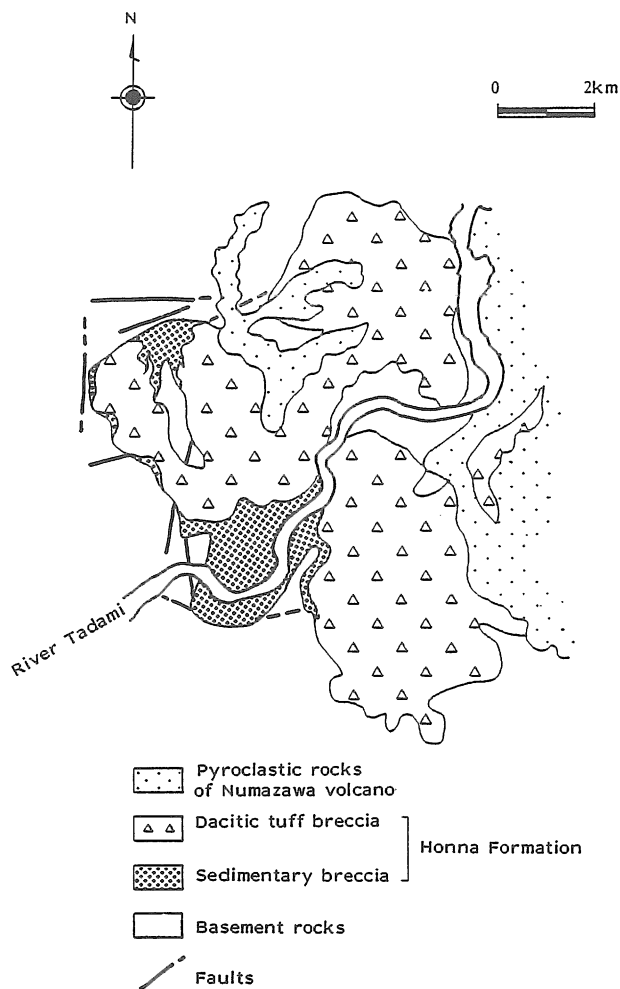
Fig. 8.   Lithofacies of the Honna Formation and structures of the basement.

Type locality: Fujitōge Pass, Yanaizu-chō, Kawanuma-gun, Fukushima Prefecture.

Stratigraphic relation: This formation conformably overlies the Shiotsubo Formation to the north of Yanaizu (SUZUKI, 1951, 1964), but it unconformably covers the Urushikubo Formation in the area from Yanaizu to Ōmine where the Shiotsubo Formation is not found.   The relation between this formation and the Sunagohara Formation may be conformable or partly interfingered, as inferred from the succession in lithofacies.

Thickness: 150 m.

Lithofacies: This formation consists of pebble conglomerates, fine tuffs, and

massive pumice tuffs, in ascending order.   The conglomerate beds contain well-sorted pebbles, and they thin northward.   The fine tuffs show fine lamination and include pisolites.   They resemble the upper Sunagohara Formation in lithofacies.   Pumice tuff beds containing exotic rock fragments compose the major part of the formation, which corresponds to the middle part of Fujitōge Formation of SUZUKI (1964).

Many plant remains, for example, *Fagus paleocrenata* OKUTSU, *Liquidanber formosana* HANCE, *Populus aizuana* HUZIOKA and SUZUKI, *Ulmus nipponics* SUZUKI, *etc.* were reported by SUZUKI (1951, 1986) and SUZUKI *et al.* (1977a, b).   A radiometric age of 1.8 Ma (K-Ar) was given by SUZUKI *et al.* (1986).

II-2.   Geologic Structure

Short vertical faults are observed around the Sunagohara and Honna Formations (Figs. 5, 6, 8).   These faults strike concordantly with the outlines of these formations, but some faults strike perpendicularly.   They develop mainly at the corner of the margin.   These faults are covered by the Sunagohara or Honna Formation.   The amount of the fault displacement cannot be estimated precisely, but they may not be so large.   These faults seem not to be controlled by any regional tectonic trends, because their strikes are not concentrated to one direction.

The flexure limb observed to the southwest of Sunagohara dips 50° to 60° NE, and its axis changes in direction from northwest to north along the margin of the Sunagohara Formation.   Its vertical displacement is about 300 m.   Anticlinal and synclinal axes with a NW–SE trend are found to the south of Sunagohara.   These folds and the flexure are unconformably covered by the Sunagohara Formation.

Two cauldrons are recognized in the Sunagohara and Honna areas as inferred from the stratigraphic and structural evidence (see chapter III).

II-3.   Correlation

Table 1 shows the correlation of the late Cenozoic formations in the Tadami-Aizu region.

The Urushikubo Formation yields the foraminiferal assemblage of Blow's N. 10 to N. 12 (SUZUKI *et al.,* 1972) or N. 9 to N. 10 (HAYAKAWA *et al.,* 1972).   The Shiotsubo Formation which conformably overlies the Urushikubo Formation yields the Yama fauna and is assigned to the upper Miocene (OTSUKA, 1941).   SHIMADA and IZAWA (1969) correlate the Matsuzakatōge Formation in the Tadami-Kobayashi region with the Shiotsubo Formation by fossil evidence.   The Matsuzakatōge Formation also conformably overlies the underlying formation.   The Fujitōge Formation conformably overlies on the Shiotsubo Formation, and is assigned to the upper Miocene to lower Pliocene (SUZUKI *et al.,* 1977a, b, 1986).

The lower Fujitōge Formation conformably overlies the upper Sunagohara Formation partly with interfingering relationship.   Accordingly, the Sunagohara Formation is correlated with the lower Fujitōge Formation, or that the upper and the lower part of

the Sunagohara Formation are assigned to the lower Fujitōge and the Shiotsubo Formations, respectively.

The Honna Formation unconformably covers the Urushikubo and Takisawagawa Formations, and is well consolidated.   It may be also of the same stratigraphic horizon as the Sunagohara Formation.

III.   STRUCTURE OF THE SUNAGOHARA AND HONNA CAULDRONS AND THE PRECEDING UPLIFT

III-1.   Structure of the Sunagohara and Honna Cauldrons

The Sunagohara and Honna Formations consist mainly of volcaniclastic and volcanic rocks, and abut on the peripheral basements.   The sedimentary basins of these formations show rectilinear polygonal outlines with 5 km in diameter, because they are bounded by steep clinounconformity surfaces with straight strikes.   These formations are cauldron fills.   The author calls these Tertiary basins of volcanic origin 'the Sunagohara cauldron' and 'the Honna cauldron', respectively.

Boundary structure of the cauldrons   The relationship between these cauldron fills and the basement is not fault contact but unconformity.   However, vertical faults are observed in the basement near the margin of the Sunagohara and Honna cauldrons (Figs. 6, 7, 8).   These faults are not arcuate but straight, and strike either in parallel or perpendicular to the cauldron margin.   They are covered by the cauldron fills.   A flexure is observed at the southwestern margin of the Sunagohara cauldron, which strikes in parallel to the margin of the cauldron with a notable displacement down to the cauldron.   It is also covered by the cauldron fills.

These vertical faults and the flexure were possibly produced relating to failure of the basements during cauldron formation.   This fracture system is concordant with the irregular polygonal outlines of the cauldrons.   Accordingly, the steep surfaces of the unconformity bordering these cauldrons may originate in these vertical faults.   It is likely that many other faults were also produced relating to the collapse, although they are concealed by the cauldron fills.   Accordingly, the location of the cauldrons coincides with the concentragted area of faults.

Sedimentary breccias   Sedimentary breccias are observed along the margin of these cauldrons (Figs. 6, 7, 8).   These breccias are scarcely stratified and disappear laterally into intracauldron tuffs.   The rock fragments are poorly sorted, and the matrix consists of the same material as the fragments.   Large blocks derived from the just underlying basements are also included.   Therefore, these breccias are interpreted to be talus deposits that accumulated on the foot of normal fault scarps surrounding the caldera depressions.   The sedimentary breccias possibly accumulated concurrently with volcanic activity as inferred from interfingering relation of these breccias and tuffs filling the cauldrons.

Pyroclastic and volcanic rocks filling the cauldrons   The basal part of the Sunago-

hara Formation consists of perlitic tuff breccias.   The lower part of this formation is composed of fine tuffs partly with slump bedding.   The upper part consists of well laminated fine tuffs, which are regarded as lake deposits as inferred from occurrence of plant and pollen remains as well as from the lithofacies.   Perlite lavas are mainly intercalated in the upper fine tuffs and partly in the lower part.   Accordingly, the Sunagohara Formation consists mainly of acidic volcaniclastic rocks and lavas except for the marginal facies.   The Honna Formation also consists of volcaniclastic rocks (dacitic tuff breccia) and marginal sedimentary breccias, but fine tuffs are not observed.   Most of these cauldron fills abut on the unconformity surface, but a part of the upper Sunagohara Formation lies on the basement.

Collapse displacement   The vertical displacement of the Sunagohara cauldron is estimated to be more than 150 m.   It is evaluated on the basis of the thickness of the cauldron fills abutting on the unconformity surface.   The vertical displacement of the Honna cauldron is also estimated to be about 200 m.   Accordingly, the scale of both cauldrons attains to 5 km in diameter and 150–200 m in throw.

III–2.   Domal Rise before the Formation of the Cauldrons

The Sunagohara and Honna Formations are assigned to the upper Shiotsubo or the lower Fujitōge Formations.   The Sunagohara and Honna Formations unconformably overlie the Urushikubo and the underlying formations, but they do not cover the Shiotsubo Formation.   The southern limit of the Shiotsubo Formation, where conglomerates are intercalated, may coincide with margin of the sedimentary basin of this formation.   The Shiotsubo Formation was probably not deposited near the cauldrons.

Distribution of the Shiotsubo Formation and the contemporary formations are shown in Fig. 9.   Accordingly, a local uplift, which was a domal rise with a diameter of about 25 km, emerged during the deposition of the Shiotsubo Formation.   Since the Sunagohara Formation unconformably covers the Ōtani Formation, the amount of the erosion may be about 250–400 m which is the thickness of the Urushikubo Formation.

The Sunagohara and Honna cauldrons were produced on this domal rise.   Generally, horizontal extension is yielded around the crest of an uplift and is accommodated by normal faults, which results in collapse of the roof of the uplift.   Accordingly, it is likely that the Sunagohara and Honna cauldrons were formed by such fault movements associated with uplifting.   Moreover, the closed polygonal outline of the cauldrons suggests that this uplift was a domal rise.   If the uplift was elongated to one direction, the resultant collapse would become a graben.

The distance between the margins of the Sunagohara Formation and the Shiotsubo Formation is less than about 5 km.   Since this cauldron is about 5 km in diameter, if the center of the dome is situated in the cauldron, the dome radius is estimated to be about 7.5 km.   However, the uplift shown in Fig. 9 is about 25 km in diameter.   It may have been produced by merging of the two domal rises.   Accordingly, the dome is concluded to be 15 to 25 km in diameter.
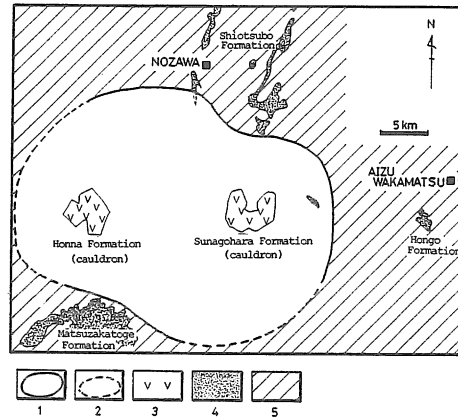
Fig. 9. Distribution of the uppermost Miocene beds and the local uplift estimated from the extent of the local unconformity.
1: area of domal rise, 2: estimated area of domal rise, 3: cauldron fills of uppermost Miocene, 4: uppermost Miocene beds in marine origin, conformably overlying the middle Miocene, 5: estimated marine area in the latest Miocene.

The Shiotsubo and the contemporary formations, which accumulated concurrently with the doming, consist mainly of non-volcanic sedimentary rocks of marine origin. This suggests that volcanism scarcely occurred during the doming.   Subsequent to the formation of the cauldrons, intense volcanic eruptions occurred in this area.   It is likely that the uplift was caused by the ascent of a magma reservoir.   The domal shape of the uplift also supports that the uplift was originated by the ascending magma.

III–3.   Eruption subsequent to the Subsidence of the Cauldrons

If the eruption began before the collapse, the lower part of the Sunagohara Formation would have extended outside the caldera, resting on the basement Tertiary rocks, and the relationship between the cauldron fills and the basement rocks would not be unconformity but fault contact.   However, the main part of the Sunagohara Formation is nearly horizontal and abuts on the steeply dipping unconformity surface.   Only a part of the uppermost fine tuffs of this formation extends outside the caldera, where it gently lies on the basement rocks.   However, the lower part of this formation is not found outside the cauldron.   These facts suggest that the eruption began after the caldera collapse.

The slump bedding of the lower Sunagohara Formation may have been formed by some differential subsidence due to minor faulting which continued up to the beginning of eruption.   However, since the bedding of the upper Sunagohara Formation is not disturbed, the fault activity should have completely ceased until the latter stage of eruption.

The caldera depression amounted to 5 km in diameter and 150–200 m in depth.

This collapsed volume may have been compensated by the horizontal extension caused by doming.

III–4. Eruption Sequence in the Sunagohara Cauldron

The Sunagohara Formation consists of tuff breccias, fine tuffs partly distrurbed by slump bedding, laminated fine tuffs and perlite lavas, roughly in ascending order. Namely, coarse pyroclastic ejecta effused first, then fine ashes were ejected. Perlite lavas flowed out mainly in the last stage of the volcanism, though minor lavas were intercalated in the lower part of this formation. It is evident that the early volcanism was most violent, which can be interpreted as due to the excess magma pressure and the reaction between magma and caldera lake water.

IV. FORMATION PROCESS OF THE SUNAGOHARA
AND HONNA CAULDRONS

IV–1. Sequence of the Formation of the Sunagohara and Honna Cauldrons

As illustrated in Fig. 10, the field evidence concerning the formation of the Sunagohara and Honna cauldrons is summarized in the following sequence:

(i) A domal rise which was caused by the ascent of a magma reservoir emerged in the late Miocene sedimentary basin (Fig. 10–I). Horizontal extension caused by doming was accommodated by normal to vertical faults.

(ii) A complicated polygonal caldera was produced due to subsidence accompanied by faulting at the top of the rising dome, so that a caldera lake appeared. Sedimentary breccias of talus origin were deposited along the caldera rim (Fig. 10–II).

(iii) Then, intense volcanic activity began in the caldera due to emission of the magma through the fractures formed during the doming and collapse. Talus accumulation continued concurrently with volcanic activity. Acidic volcaniclastic material filled the caldera, and they became finer in the later stage. Most of the perlite lavas flowed out in the last stage (Fig. 10–III).

IV–2. Comparison with the Motojuku Cauldron

The Sunagohara and Honna cauldrons are partly similar to the Motojuku cauldron in the formation sequence and structures as illustrated in Fig. 11.

According to FUJITA et al. (1970), the process of the formation of the Motojuku cauldron is summarized as follows: (1) Domal rise caused by ascending of a magma reservoir. (2) Caldera collapse (primary collapse). Horizontal extension due to up-warping of the dome was accommodated by normal faults, and the roof of the dome collapsed to form a caldera of 12 km across with a polygonal outline, roughly triangular in shape. (3) Accumulation of sedimentary breccia on the foot of the normal fault scarps. (4) & (5) The caldera was filled with pyroclastic materials, marginal sedimentary breccias of talus origin, and lake deposits. (6) Thick andesite lavas flowed
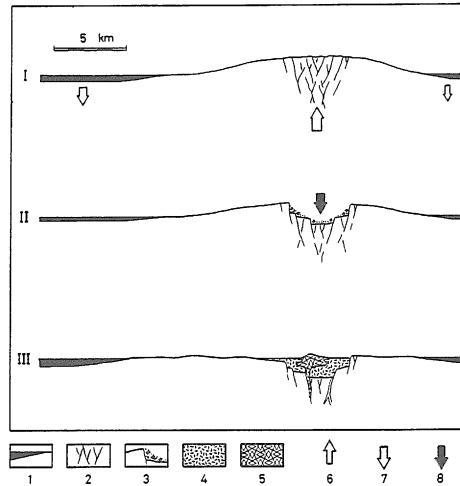
Fig. 10.   Cartoon illustrating the formation process of the Sunagohara cauldron.
          I: Subsidence of the late Miocene marine basin continuously from the middle
          Miocene and domal rise caused by the ascending magma reservoir.   Many normal
          and vertical faults were produced near the crest of the dome.   II: Caldera collapse
          along the normal faults and deposition of sedimentary breccia mainly along the
          caldera rim.   III: Eruption of acidic ash and subsequent outpouring of perlitic lava.
          The sequence of the formation of the Honna cauldron is essentially same as this
          scheme.
          1: marine basin (mainly of normal sediments except the margin of the dome),
          2: faults, 3: sedimentary breccia, 4: acidic fine tuff, 5: perlite lava, 6: uplift,
          7: subsidence, 8: collapse.

out near the central part of the cauldron.   (7) Subsequent to the voluminous outpouring
of andesite lavas, the secondary collapse occurred in the cauldron.   This collapse
structure is observed as a circular flexure with a diameter of 4 km and a vertical
displacement of 800 m on the surface.   (8) & (9) Many intermediate to acidic dikes and
plutonic rocks intruded into the cauldron.   Some of them were regarded as cone sheets.

Since this process was first established at the Motojuku cauldron, this type of
cauldrons is called 'the Motojuku type cauldrons'.   Fujita (1972) showed that many
other cauldrons of this type were produced in the Green Tuff region during the
Miocene.

It is noticed that the Motojuku type cauldron is characterized by (1) the polygonal
outline associated with the development of normal to vertical faults on the apex of the
rising dome, (2) the cauldron collapsed before the main eruption, and (3) the secondary
collapse after the voluminous outpouring of lavas.   The later events such as the
secondary collapse and the intrusion of plutonic rocks, are not observed in the
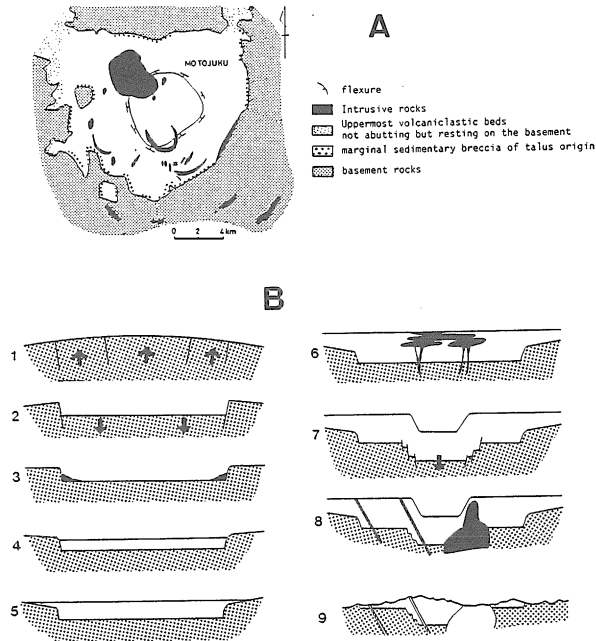Sunagohara and Honna cauldrons.

Fig. 11. Structural map (A) and tectonic process (B) of the Motojuku cauldron (simplified from FUJITA *et al.*, 1970).
1: faulting produced by extension on a dome apex, 2: caldera collapse with a diameter of 12 km and a depth of 500 m (the primary collapse), 3: accumulation of sedimentary breccia at the foot of normal fault scarps, 4: beginning of pyroclastic eruption in the caldera, 5: continuous eruption and overflowing accumulation of volcaniclastics, 6: voluminous outpouring of lava near the center of the cauldron, 7: the secondary collapse of 4 km in diameter with a depth of 800 m, 8: intrusion of volcanic dikes and plutonic rocks, 9: present section.

V. NUMERICAL ANALYSES AND MODEL EXPERIMENTS OF THE FORMATION OF CAULDRON

This chapter is concerned with the following several problems.

The first problem is how to determine the depth and size of the magma reservoir which caused a domal uplift.   The diameter of the dome is estimated to be 15–25 km in this region, probably 20 km in average (Fig. 12).   FUJITA *et al.* (1974) and KOMURO *et al.* (1977) reported that the diameter was about 30 km in the case of the cauldron found in the eastern Aizu district of Northeast Japan.   FUJITA *et al.* (1970) estimated it to be 60–70 km in diameter in case of the Motojuku cauldron.   This may be one of the largest domes preceding to the formation of the Motojuku type cauldron.   Accordingly, the diameters of the preceding domes of the Motojuku type cauldrons are probably 30 km in average, and not more than 70 km.   The uplift of the dome may amount to several
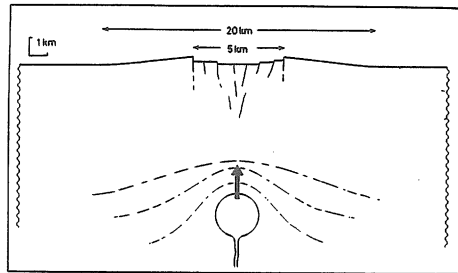
Fig. 12.   A model of an ascending magma reservoir with the size of the surface dome and
          cauldron.

hundred meters.   However, the depth and the size of the magma reservoir are re-
mained as unknown factors.

The second problem is how to estimate the amount of collapse.   The collapse
displacement of the Sunagohara cauldron may be about 200 m as mentioned earlier.
FUJITA *et al.* (1970) estimated it at about 500 m in the Motojuku region.   In these cases,
a volume of 4–57 km^3 (5–12 km across by 200–500 m deep) was lost by collapse before
the main eruption.   Accordingly, the problem is whether or not the collapsed amount
of several hundred meters was compensated by extension on the dome apex.   General-
ly, a horizontal tensile stress field dominates at the top of a dome and eventually leads to
collapse as ascertained in model experiments by previous workers (CURRIE, 1956;
PARKER and MCDOWELL, 1956; SANFORD, 1959).   However, these model experiments are
not concerned with the amount of the collapse.   We need to confirm whether or not the
collapsed amount of the model experiments coincides with the observational facts which
is evaluated at several hundred meters in depth.

The third problem is how to examine the size of the cauldron.   Many cauldron
have a diameter of 5–10 km.   What is the factor to determine this dimension?   BONIN
(1985) pointed out that the caldera radius is in proportion to the size of the magma
reservoir.   Can we accept his conclusion?

The above problems cannot be solved by field works.   In order to investigate these
problems, the author tried to simulate the formation process of the cauldron by means
of finite element analyses and scale model experiments.

Since scale model experiments are constrained by physical similarity, difficulties lie
in selection of model materials and time scales for experiments.   However, because
model experiments do not require a knowledge of physical equations that control a
tectonic system, they can be applied to such a problem as discontinuous failure for which
physical equations have not been determined.   Finite element analysis (FEM), on the
other hand, is an effective method for analyzing continuous deformation which is
described by numerical equations.   Therefore, the author performed simulations by the
use of FEM to investigate continuous deformation problem and scal model experiments
to examine discontinuous failure problem.

Prior to give numerical and experimental descriptions, the characters of an ascending magma reservoir are discussed.

V-1. Magma Reservoir

Many workers tried to confirm the existence of the reservoir by means of geological (e.g. RITTMANN, 1936) and geophysical methods (e.g. GORSHKOV, 1958; MOGI, 1958). GORSHKOV (1958) observed missing of shear waves which passed under the volcanoes of the Klyuchevskaya group.   A magmatic body with a diameter of 25–35 km at a depth of 50 to 70 km appeared to have absorbed shear waves traveling through this zone.   A similar work was carried out by KUBOTA and BERG (1967) in the Katmai volcanic region, Alaska Peninsula.   They found about ten shallow magma reservoirs (20 km in maximum depth) corresponding to each of the active volcanoes in this region.

EATON et al. (1975) observed a zone of attenuation for compressive seismic waves, in which shear waves were absent on some records, under Yellowstone caldera.   They interpreted the delay-producing body as a shallow silicic magma body with 20–30 km in horizontal diameter connecting with a deep root which is possibly partly molten. KOYANAGI and ENDO (1976) inferred a reservoir with 3–6 km in depth and 2–3 km in diameter below Kilauea volcano from the absence of earthquake hypocenters.

MOGI (1958) observed vertical displacements of the ground surface around Sakurajima volcano before and after the 1914 eruption by means of the precise leveling and triangulation.   A limited area close to the crater was upheaved locally, but a wide circular area including the Kagoshima Bay, centered on 10 km north from the present crater, was subsided.   He inferred that the extent of the deformed area depended on the depth of a forced point; the local upheaval around the crater was caused by the shallow origin, whereas the wide depression by the deeper origin.   He estimated the depth of the magma reservoir below Sakurajima volcano at 10 km by the application of elastic theory.

As mentioned above, most of the workers considered that magma reservoirs are situated at a shallow level in the crust.   Morevoer, the author assumes that the magma reservoir which caused a domal rise should have a certain volume and stiffness.

The shape of a magma body which rises by buoyant force was simulated by model experiments.   Plate II–1 and II–2 show model experiments of diapir evolution of two viscous layers.   A tight-rectangular acrylic-glass box $(10 \times 15 \times 25 \text{ cm})$ was filled completely with the source buoyant layer of silicone oil and the overburden layer of syrop. The source layer was 0.5–0.6 cm thick, density 0.98 g/cm^3 and viscosity 1.1×10^2 Pas, while the overburden layer was density of 1.36 and 1.49 g/cm^3 and viscosity of 9.75 and 3.0×10^3 Pas.   When the oil stabilized itself as a uniform layer over the overburden fluid, the box was turned upside down and the diapir evolution from this unstable situation was observed.

Dynamic similarity of the model is given according to EMORI (1985).   Buoyant force F_b and viscosity force F_v are expressed by representative parameters as

$$F_b = \Delta\varrho gl^3 \tag{1}$$

$$F_v = \eta l^2 t^{-1} \tag{2}$$

respectively. Where, $\Delta\varrho$: density difference between the two layers, g: gravity acceleration, l: length, η: viscosity, t: time. As we can ignore the Reynold's number because of the slow deformation, the pi-number of the model is as follows:

$$\Pi = F_b/F_v = \Delta\varrho glt/\eta \tag{3}$$

The pi-number must have the same value between original and model. Assigning the subscript m and o to the model and prototype, respectively, the relation of control parameters is written by

$$\Delta\varrho_o g_o l_o t_o/\eta_o = \Delta\varrho_m g_m l_m t_m/\eta_m \tag{4}$$

Referring subscript r to the model ratio,

$$\eta = \Delta\varrho_r g_r l_r t_r \tag{5}$$

Substituting the following value into these control parameters,

$\Delta\varrho_r = 1.0$
$g_r = 1.0$
$l_r = 10^{-5}$
$t_r = 10$ (minutes)/1 (Ma) $= 1.9 \times 10^{-11}$

we get the following viscosity ratio,

$$\eta_r = 1.9 \times 10^{-16} \tag{6}$$

If we accept a value 10^{19} Pas for the viscosity of the lower crust, the overburden syrop of the model $(1.9 \times 10^3$ Pas) corresponds to the earth's crust in viscosity. When the viscosity contrast between the overburden and the buoyant layers was 27/1, the following process was observed.

On the originally plane but gravitationally unstable source layer surface, waves started to form and their amplitude increased very slowly at first. Soon later, culminations began to change the waves into spherical diapirs which rose rapidly through the overburden layer. It is noted that each diapir formed a certain mass of sphere. As the diapir approached the upper roof of the box, rising velocity of the diapir gradually decreased and laterally expanded. Most of the diapirs ceased to rise about 30 minutes after the start of the test.

Plate II-2 shows another experiment which consists of a buoyant oil layer 0.5 cm thick with viscosity 1.1×10^2 Pas and an overburden with 9.75 Pas. Namely, the viscosity ratio between the overburden and the byoyant layer was 0.09/1. The viscosity of the overburden was less in contrast than the previous model (Plate II-1). The diapirs were small in diameter and showed not spherical but vertically elongated shapes.

Accordingly, if the diapir whose viscosity is less than that of the crust ascends from the source layer, it forms not an elongated but spherical shape.   Therefore, if a liquid or partially melting magma reservoir rises by buoyant force, it is reasonable that the reservoir is assumed to be a sphere.   Moreover, according to OLSON and NAM (1986), even if the ascending reservoir is low in viscosity, it can swell the free surface of high-viscosity overburden.

V–2.   Numberical Analyses on the Scale of Surface Dome
V–2–1.   Elasto-plastic deformation

A domal uplift is assumed to be large deformation that remains permanent plastic strain.   No viscous flow is recognized around the dome, but faulting, discontinuous failure of the crust, is remarkable.   Therefore, in this model the crust is assumed to be an elasto-plastic body which has no relation to strain rate.

Elastic deformation is described by infinitesimal strain equations.   Although plasticity is finite deformation, it can be analyzed as incremental deformation of infinitesimal elastic strain.

Strain beyond elastic limit consists of elastic and plastic components (Fig. 13). This stress-strain relation is similar to that of rock deformation.   When external load is taken away, elastic strain is returned to zero, but plastic strain remains.   This means that plastic strain is regarded as permanent deformation or dislocation.   Microfractures in rock or faults in the earth's crust are interpreted as the permanent dislocation. Accordingly, the author supposes that plastic deformation represents not only continuous permanent deformation but also faulting as discontinuous failure.

Constitutive equation of isotropic linear elasticity is described in matrix form with Young's modulus E and Poisson's ratio ν as follows:

$$\{\sigma\}=[D_e]\{\varepsilon\} \tag{7}$$

or

$$
\begin{bmatrix} \sigma_x \\ \sigma_y \\ \sigma_z \\ \tau_{yz} \\ \tau_{zx} \\ \tau_{xy} \end{bmatrix}
= \frac{E}{1+\nu}
\begin{bmatrix}
\dfrac{1-\nu}{1-2\nu} & \dfrac{\nu}{1-2\nu} & \dfrac{\nu}{1-2\nu} & 0 & 0 & 0 \\[2mm]
\dfrac{\nu}{1-2\nu} & \dfrac{1-\nu}{1-2\nu} & \dfrac{\nu}{1-2\nu} & 0 & 0 & 0 \\[2mm]
\dfrac{\nu}{1-2\nu} & \dfrac{\nu}{1-2\nu} & \dfrac{1-\nu}{1-2\nu} & 0 & 0 & 0 \\[2mm]
0 & 0 & 0 & \dfrac{1}{2} & 0 & 0 \\[2mm]
0 & 0 & 0 & 0 & \dfrac{1}{2} & 0 \\[2mm]
0 & 0 & 0 & 0 & 0 & \dfrac{1}{2}
\end{bmatrix}
\begin{bmatrix} \varepsilon_x \\ \varepsilon_y \\ \varepsilon_z \\ \gamma_{yz} \\ \gamma_{zx} \\ \gamma_{xy} \end{bmatrix}
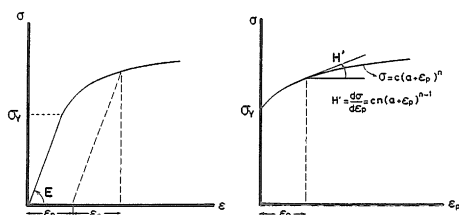\tag{7'}
$$

Fig. 13. Stress-strain curve of elasto-plastic de-
          formation.
          Left: stress and total strain relation.
          Right: stress and plastic strain relation.
          Total strain consists of elastic (ε_e) and
          plastic (ε_p) strains. E: Young's mod-
          ulus, σ_Y: yield stress (elastic limit), H':
          gradient of a strain hardening curve
          which is approximated with an ex-
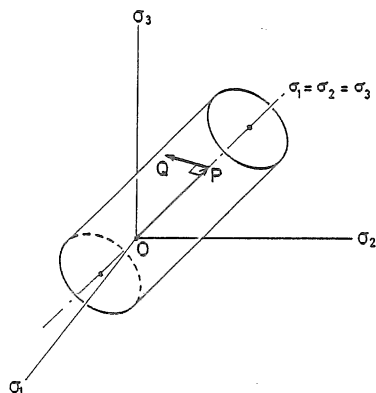   ponential curve.

Fig. 14. Von Mises' yield condition in the prin-
          cipal stress coordingate system.
          The yield condition is shown as a cylin-
          der along the axis $\sigma_1 = \sigma_2 = \sigma_3$.
          OP: hydrostatic pressure, PQ: deviat-
          ric stress. Note that PQ is constant
          despite the length of OP.

where σ_x... and ε_x... are stress and strain components, respectively.   [De] is called elastic stress-strain matrix.

For the yield condition that is critical point of elastic state, von Mises' criterion is adopted (JAEGER, 1956; YAMADA, 1980). This criterion means that yielding occurs when an equivalent stress $\bar{\sigma}$ which is expressed by

$$\bar{\sigma}=\sqrt{\frac{1}{2}\left\{(\sigma_x-\sigma_y)^2+(\sigma_y-\sigma_z)^2-(\sigma_z-\sigma_x)^2+6(\tau_{yz}^2+\tau_{zx}^2+\tau_{xy}^2)\right\}} \qquad (8)$$

exceeds a constant σ_Y.

This criterion means that $\bar{\sigma}$ corresponds to uniaxial stress σ_x if $\sigma_y=\sigma_z=\tau_{yz}=\tau_{zx}=\tau_{xy}$ $=0$.   Therefore, the yield condition of tri-axial stress is converted into scalar.   Fig. 14 shows the von Mises' criterion in the principal-stress coordinate system.   A line with equal direction cosines (l, m, n) indicates hydrostatic pressure ($\sigma_1=\sigma_2=\sigma_3$).   A cylinder of which axis coincides with this line represents the yielding surface of the Mises' criterion.   While a stress point is included within the cylinder, elastic state is maina-tined.   However, if the stress point deviates from the axis so that it penetrates the cylinder surface, material yields to become plastic state.   Namely, under this criterion, yielding bears no relation to hydrostatic pressure.   Generally, since compressive strength of rock is larger than its tensile strength, yielding surface of rock would not be cylindrical but conical or parabolic shape opened toward compressive stress.   Accor-dingly, Mises' criterion may not always represent the fracturing and yielding of rock.   However, since the hydrostatic pressure originates in overburden, mass and scale of

models can be disregarded under Mises' criterion. If the stress state is carefully analyzed, this criterion is useful because of the results with no relation to the scale effects.

Strain hardening after yielding is approximated by an empirical equation

$$\bar{\sigma} = c(a + \varepsilon_p)^n \qquad (0 \leq n \leq 1) \tag{9}$$

where c is a constant with stress dimension, a and n are dimensionless constants (Fig. 13). When n equals zero, the equation (9) means non-hardening or complete plastic material, and means linear-hardening material when n equals 1. In equation (9), substituting zero into ε_p, we get

$$\sigma_Y = \bar{\sigma} = ca^n$$

$$\therefore a = (\sigma_Y/c)^{\frac{1}{n}} \tag{10}$$

Consequently, only two physical constants, c and n, are unknown parameters.

Constitutive equation of plastic material after yielding is expressed in matrix form as follows:

$$\{d\sigma\} = [Dp] \{d\varepsilon\} \tag{11}$$

Stress and strain are described as incremental expression, because these relations are not linear in plastic deformation. $[Dp]$ is called plastic stress-strain matrix and is expressed by

$$[D_p] = [D_e] - \frac{1}{S} \begin{bmatrix} S_1^2 & S_1 S_2 & S_1 S_3 & S_1 S_4 & S_1 S_5 & S_1 S_6 \\ & S_2^2 & S_2 S_3 & S_2 S_4 & S_2 S_5 & S_2 S_6 \\ & & S_3^2 & S_3 S_4 & S_3 S_5 & S_3 S_6 \\ & & & S_4^2 & S_4 S_5 & S_4 S_6 \\ & \text{Sym.} & & & S_5^2 & S_5 S_6 \\ & & & & & S_6^2 \end{bmatrix} \tag{12}$$

where,

$$S_1 = D_{11}^e \sigma_x' + D_{12}^e \sigma_y' + D_{13}^e \sigma_z' \qquad (\sigma_x' = \sigma_x - \frac{\sigma_x + \sigma_y + \sigma_z}{3} \ etc.)$$

$$S_2 = D_{21}^e \sigma_x' + D_{22}^e \sigma_y' + D_{23}^e \sigma_z'$$

$$S_3 = D_{31}^e \sigma_x' + D_{32}^e \sigma_y' + D_{33}^e \sigma_z'$$

$$S_4 = 2D_{44}^e \tau_{yz}$$

$$S_5 = 2D_{55}^e \tau_{zx}$$

$$S_6 = 2D_{66}^e \tau_{xy}$$

$$S = \frac{4}{9}\bar{\sigma}^2 H' + S_1\sigma'_x + S_2\sigma'_y + S_3\sigma'_z + 2(S_4\tau_{yz} + S_5\tau_{zx} + S_6\tau_{xy})$$

Dij are components of $[De]$ matrix shown in equation (7). H' is strain hardening gradient and is given as follows:

$$H' = d\sigma/d\varepsilon_p = nc(a + \varepsilon_p)^{n-1} \qquad (0 \leqq n \leqq 1) \tag{13}$$

V-2-2. Method of finite element analysis

The analytical steps are as follows:

(i)   A continuous elasto-plastic two-dimensional body is divided into a number of elements of finite dimensions, for example, triangles joined together at their nodes, so that the nodes of the adjacent elements have common displacements.

(ii)   Continually changing strain in each element is dispersed into the nodal displacement.   Namely, a state of strain is commonly assumed to be constant in each element, but different from element to element.

(iii)   The stress-strain relations are used in order to obtain the stresses in the element and to find a set of fictitious nodal forces on each element, which would be in equilibrium with the internal stresses.   This procedure is an application of the theorem of minimum potential energy.
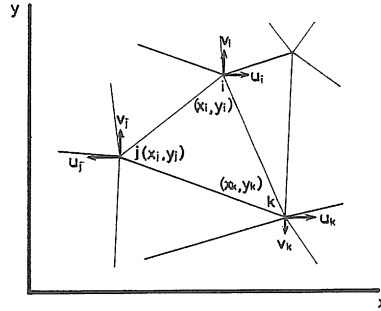

Fig. 15.   Apexes and their coordinates of a triangle element.   i, j and k are nodal numbers of the element, and u and v are the displacements in x and y directions, respectively.

Fig. 15 shows the apexes and its coordinates of a triangle element.   We can get a uniform strain state within the element, assuming the displacements u and v to be given by linear functions of x and y.   Namely,

$$u(xy) = \alpha_0 + \alpha_1 x + \alpha_2 y$$
$$v(xy) = \beta_0 + \beta_1 x + \beta_2 y \tag{14}$$

where α_0, α_1, α_2, β_0, β_1 and β_2 are constants.   These equations mean that the edges of

the elements remain straight lines after deformation. The displacements u and v are continuous from element to element, because two adjacent elements have common nodes.

The constants can be obtained in terms of the nodal displacements u_i, v_i, u_j, v_j, u_k and v_k by applying the equations (14).

$$\begin{bmatrix} \alpha_0 \\ \alpha_1 \\ \alpha_2 \end{bmatrix} = \frac{1}{\Delta} \begin{bmatrix} \Delta_{11} & \Delta_{21} & \Delta_{31} \\ \Delta_{12} & \Delta_{22} & \Delta_{32} \\ \Delta_{13} & \Delta_{23} & \Delta_{33} \end{bmatrix} \begin{bmatrix} u_i \\ u_j \\ u_k \end{bmatrix} \tag{15}$$

and

$$\begin{bmatrix} \beta_0 \\ \beta_1 \\ \beta_2 \end{bmatrix} = \frac{1}{\Delta} \begin{bmatrix} \Delta_{11} & \Delta_{21} & \Delta_{31} \\ \Delta_{12} & \Delta_{22} & \Delta_{32} \\ \Delta_{13} & \Delta_{23} & \Delta_{33} \end{bmatrix} \begin{bmatrix} v_i \\ v_j \\ v_k \end{bmatrix} \tag{16}$$

where

$$\Delta = \begin{vmatrix} 1 & x_i & y_i \\ 1 & x_j & y_j \\ 1 & x_k & y_k \end{vmatrix} \tag{17}$$

and Δ_{ij} are cofactors of determinant Δ.

The strains in the element corresponding to the displacement functions (14) are:

$$\varepsilon_x = \frac{\partial u}{\partial x} = \alpha_1$$

$$\varepsilon_y = \frac{\partial v}{\partial y} = \beta_2 \tag{18}$$

$$\gamma_{xy} = \frac{\partial u}{\partial y} + \frac{\partial v}{\partial x} = \alpha_2 + \beta_1$$

It is noted that these equations are not functions of x and y but constants. Namely, strains are constant in an element. Equations (18) can be rewritten in a matrix form as

$$\{\varepsilon\} = [B]\{u\} \tag{19}$$

or

$$\begin{bmatrix} \varepsilon_x \\ \varepsilon_y \\ \gamma_{xy} \end{bmatrix} = \frac{1}{\Delta} \begin{bmatrix} \Delta_{12} & 0 & \Delta_{22} & 0 & \Delta_{32} & 0 \\ 0 & \Delta_{13} & 0 & \Delta_{23} & 0 & \Delta_{33} \\ \Delta_{13} & \Delta_{12} & \Delta_{23} & \Delta_{22} & \Delta_{33} & \Delta_{32} \end{bmatrix} \begin{bmatrix} u_i \\ v_i \\ u_j \\ v_j \\ u_k \\ v_k \end{bmatrix} \tag{19'}$$

The coefficients in $[De]$ matrix for plane strain are

$$[D_e] = \frac{E}{1+\nu} \begin{bmatrix} \dfrac{1-\nu}{1-2\nu} & \dfrac{\nu}{1-2\nu} & 0 \\[2ex] \dfrac{\nu}{1-2\nu} & \dfrac{1-\nu}{1-2\nu} & 0 \\[2ex] 0 & 0 & \dfrac{1}{2} \end{bmatrix} \tag{20}$$

Substituting (19) into (7) leads to

$$\{\sigma\} = [D_e]\{\varepsilon\} = [D_e][B]\{u\} \tag{21}$$

or

$$\begin{bmatrix} \sigma_x \\ \sigma_y \\ \tau_{xy} \end{bmatrix} = \frac{E}{\Delta(1+\nu)} \begin{bmatrix} \dfrac{1-\nu}{1-2\nu} & \dfrac{\nu}{1-2\nu} & 0 \\[2ex] \dfrac{\nu}{1-2\nu} & \dfrac{1-\nu}{1-2\nu} & 0 \\[2ex] 0 & 0 & \dfrac{1}{2} \end{bmatrix} \begin{bmatrix} \Delta_{12} & 0 & \Delta_{22} & 0 & \Delta_{32} & 0 \\ 0 & \Delta_{13} & 0 & \Delta_{23} & 0 & \Delta_{33} \\ \Delta_{13} & \Delta_{12} & \Delta_{23} & \Delta_{22} & \Delta_{33} & \Delta_{32} \end{bmatrix} \begin{bmatrix} u_i \\ v_i \\ u_j \\ v_j \\ u_k \\ v_k \end{bmatrix} \tag{21'}$$

which means that the stresses in the element are now written in terms of the nodal displacements.

For plane stress conditions in a continuum, and with point forces only on the boundary, the virtual work equation is written in incremental form as follows:

$$\iiint_{\mathfrak{D}} \llcorner \delta\varepsilon \lrcorner \{\delta\sigma\} dxdydz - \llcorner \delta u \lrcorner \{\delta P\} = 0 \tag{22}$$

or

$$\iiint_{\mathfrak{D}} (\delta\sigma_x \delta\varepsilon_x + \delta\sigma_y \delta\varepsilon_y + \delta\tau_{xy}\delta\gamma_{xy}) dxdydz$$

$$- \llcorner \delta u_i \ \ \delta v_i \ \ \delta u_j \ \ \delta v_j \ \ \delta u_k \ \ \delta v_k \lrcorner \begin{bmatrix} \delta f_i \\ \delta g_i \\ \delta f_j \\ \delta g_j \\ \delta f_k \\ \delta g_k \end{bmatrix} = 0 \tag{22'}$$

where δf and δg are incremental nodal (external) forces in x and y directions, and $\delta\varepsilon_x$...

and $\delta u_i...$ are incremental strain and displacement components, respectively. Substituting (21) into (22), we get

$$\iiint_{\mathfrak{D}} \lfloor \delta u \rfloor [B]^T [D] [B] \{\delta u\} dx dy dz - \lfloor \delta u \rfloor \{\delta P\} = 0 \qquad (23)$$

Since stress and strain are constant over the element, equation (23) can be changed into

$$\lfloor \delta u \rfloor [B]^T [D] [B] \{\delta u\} \iiint_{\mathfrak{D}} dx dy dz - \lfloor \delta u \rfloor \{\delta P\} = 0$$

$$\therefore Sh \lfloor \delta u \rfloor [B]^T [D] [B] \{\delta u\} - \lfloor \delta u \rfloor \{\delta P\} = 0 \qquad (24)$$

where S and h are the area and thickness of the elesment, respectively. S equals $\Delta/2$. If $Sh[B]^T[D][B]$ is replaced with $[K]$, equation (24) is expressed as

$$[K]\{\delta u\} = \{\delta P\} \qquad (25)$$

or

$$
\begin{bmatrix}
K_{11} & K_{12} & K_{13} & K_{14} & K_{15} & K_{16} \\
K_{21} & K_{22} & K_{23} & K_{24} & K_{25} & K_{26} \\
K_{31} & K_{32} & K_{33} & K_{34} & K_{35} & K_{36} \\
K_{41} & K_{42} & K_{43} & K_{44} & K_{45} & K_{46} \\
K_{51} & K_{52} & K_{53} & K_{54} & K_{55} & K_{56} \\
K_{61} & K_{62} & K_{63} & K_{64} & K_{65} & K_{66}
\end{bmatrix}
\begin{bmatrix}
\delta u_i \\
\delta v_i \\
\delta u_j \\
\delta v_j \\
\delta u_k \\
\delta v_k
\end{bmatrix}
=
\begin{bmatrix}
\delta f_i \\
\delta g_i \\
\delta f_j \\
\delta g_j \\
\delta f_k \\
\delta g_k
\end{bmatrix}
\qquad (25')
$$

$[K]$ is called element stiffness matrix, which consists of 6×6 components.   Introducing the followisng matrix and vectors on each node,

$$K_{ii}^m = \begin{bmatrix} K_{11} & K_{12} \\ K_{21} & K_{22} \end{bmatrix} \quad K_{ij}^m = \begin{bmatrix} K_{13} & K_{14} \\ K_{23} & K_{24} \end{bmatrix} \quad etc.$$

$$\delta \vec{u}_i = \begin{bmatrix} \delta u_i \\ \delta v_i \end{bmatrix} \qquad etc. \qquad (26)$$

$$\delta \vec{f}_i = \begin{bmatrix} \delta f_i \\ \delta g_i \end{bmatrix} \qquad etc.$$

equation (25′) is changed into

$$
\begin{bmatrix} K_{ii}^m & K_{ij}^m & K_{ik}^m \\ K_{ji}^m & K_{jj}^m & K_{jk}^m \\ K_{ki}^m & K_{kj}^m & K_{kk}^m \end{bmatrix} \begin{bmatrix} \delta\vec{u}_i \\ \delta\vec{u}_j \\ \delta\vec{u}_k \end{bmatrix} = \begin{bmatrix} \delta\vec{f}_i \\ \delta\vec{f}_j \\ \delta\vec{f}_k \end{bmatrix}
\tag{27}
$$

Adding the matrix elements to the position of each node, we get the overall stiffness matrix.

$$
K_{ij} = \sum_m K_{ij}^m, \qquad \delta u_i = \sum_m \delta u_i, \qquad \delta f_i = \sum_m \delta f_i
$$

Consequently,

$$
\begin{bmatrix} K_{11} & K_{12} & \cdots & K_{1,2n} \\ K_{21} & K_{22} & \cdots & K_{2,2n} \\ \vdots & & & \\ K_{2n,1} & & \cdots & K_{2n,2n} \end{bmatrix} \begin{bmatrix} \delta u_1 \\ \delta u_2 \\ \vdots \\ \delta u_{2n} \end{bmatrix} = \begin{bmatrix} \delta f_1 \\ \delta f_2 \\ \vdots \\ \delta f_{2n} \end{bmatrix}
\tag{28}
$$

Therefore, overall stiffness equations are $2n$ simultaneous equations with $2n$ unknown variables.

These equations are solved by conjugate gradient method which is a kind of iterative methods in numerical analayses. We can get a numerical exact solution except for rounded error by this method.

Approximation of this analyses is embedded in equation (14). It is assumed that strain is uniformly distributed in one element and discontinuously changes to the next element. Equations (18) show that strain components described by differentiation of displacements are rewritten to simple constants according to assumption of equation (14). Namely, the accuracy of this analysis depends on the element size. If we divide the part where strain concentration is expected into smaller elements, we can get more accurate results.

V-2-3. Boundary conditions

A simplified section model is analyzed as a plane strain problem. The boundary conditions of the model are shown in Fig. 16. The model is symmetrical, and consequently only one half of it is analyzed by the finite element method.

The effect of an ascending magma reservoir is given by the displacements of external loads at the boundary nodes, not by stress or pressure. A convex forced displacement with width B and amount of displacement H is given to the basal part of the homogeneous crust section, which has total length L and thickness D (D is regarded as depth of the apex of a magma reservoir). W and H' are the width and the vertical displacement of a dome, respectively, which are not initial parameters but results of
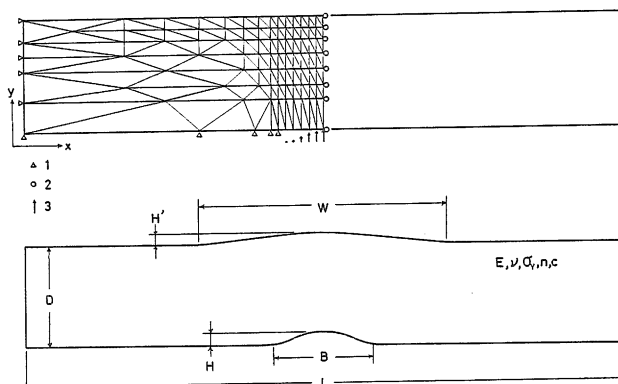
Fig. 16. Boundary conditions and triangle elements.
1: fixed nodes, 2: fixed only in x direction, free in y direction, 3: external
displacement in y direction.   Parameter names are shwon in Table 2.

tests.   However, only W and H' are known factors obtained from geological data.

The initial stress originated from the body force of gravity is assumed to be in the state of hydrostatic pressure ($\bar{\sigma}=0$).   This initial stress does not increase in the later stages of deformation, because it is the function of depth.   Therefore, it is ignored in the calculation of equivalent stress $\bar{\sigma}$, and has no relation to yielding under Mises' criterion.

Five physical constants are derived from elasto-plastic equations.   Young's modulus E and Poisson's ratio ν are derived from elastic equations.   Yield strangth σ_Y is the constant of equation (8). c and n come from the equation (9) of strain hardening rate (Table 2, 3).

Accordisng to SHIMAMOTO (1974), the complete equation of this system with these parameters is expressed as

$$f_1[\varepsilon_{ij}, L, B, D, H, E, \nu, \sigma_Y, c, n]=0 \tag{30}$$

Table 2.   Parameters of numerical analyses.

		Parameter Name	Dimension
Shape Parameters	L	Overall Length	L
	B	Size of the Basal Deformation	L
	D	Thickness of the Layer	L
	H	Displacement of the Basal Deformation	L
Physical Constants	E	Young's Modulus	$ML^{-1}T^{-2}$
	ν	Poisson's Ratio	Dimensionless
	σ_Y	Yield Stress	$ML^{-1}T^{-2}$
	c	Coefficient of Strain Hardening	$ML^{-1}T^{-2}$
	n	Exponent of Strain Hardening	Dimensionless

Table 3.   Numerical models (N-series) and controlled parameters.

	H'/D	H'/B	B:D
Model N-1	0.001 ~ 0.094		2:1
Model N-2A		0.0175	20: 3 20: 6 20:12 20:18 20:30
Model N-2B	0.01		33:30 20:30 8:30

where ε_{ij} is strain component at an arbitrary point in the system.   Since the rank of the dimensional matrix of this equation is two, by taking length and stress as two basic parameters, strain components are expressed by transforming equation (31) as follows:

$$\varepsilon_{ij} = f_2[B/L \quad H/D \quad B/D \quad \sigma_Y/E \quad \nu \quad \sigma_Y/c \quad n] \tag{31}$$

If we assume $L \gg B$, we get $B/L \doteqdot 0$.   As a resuslt, the system is completely controlled by two geometric parameters ($H/D, B/D$) and four physical parameters (σ_Y/E, ν, σ_Y/c, n).

Model N–1 and N–2, as shown in Table 5–2, are designed according to the two parameters, H'/D and B/D.

Model N–3 is planned in order to analyze the effect of the spacing of reservoirs (Fig. 17).   In Model N–3, the reservoirs ascend without volume change, and the ratio of the diameter of the reservoir to its depth is 0.27.   The ratio of the distance to the depth of the reservoirs is the only controlled parameter, which takes 4/3 and 3/2.
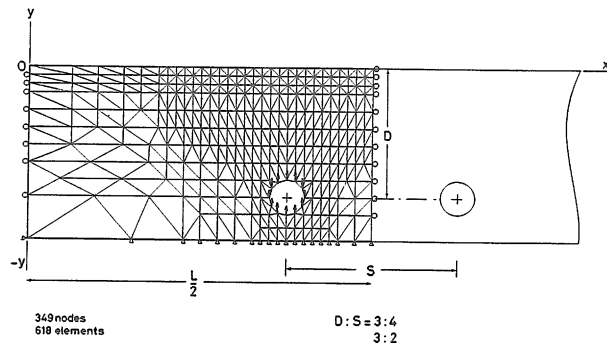

Fig. 17.   Boundary conditions and triangle elements of Model N–3.   Forced displacement in y direction is given along the circumference of a magma reservoir circle.   Two test cases, D: S=3:4 and 3:2, are planned.

V–2–4.   Results of analyses

V–2–4–(a).   Effect of the rise of a magma reservoir on the surface deformation (Model N–1)

Fig. 18 shows the progress of the surface uplift caused by the convex lifting at the base of the model layer when parameter B is constant.   Vertical displacement (H') increases with lifting, whereas the width of the domal rise (W) remains almost constant, during the range of H'/D less than 9.4%.

Shear strain just under the surface is small enough to be neglected, because the boundary condition of the surface is free.   Consequently, $x-y$ strains at the surface are nearly equal to the principal strains.   Fig. 19 shows the change of horizontal strains ε_x at the earth's surface.   The amount of horizontal strain increases, but the area of tensile
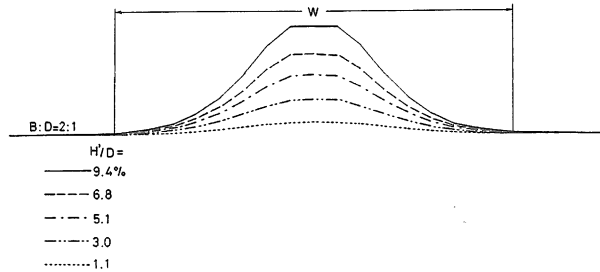
Fig. 18.   Model N-1.   Progress of the surface uplift.   The vertical displacement H′ is
shown ten times as large as the actual size.   Note that the diameter of the surface
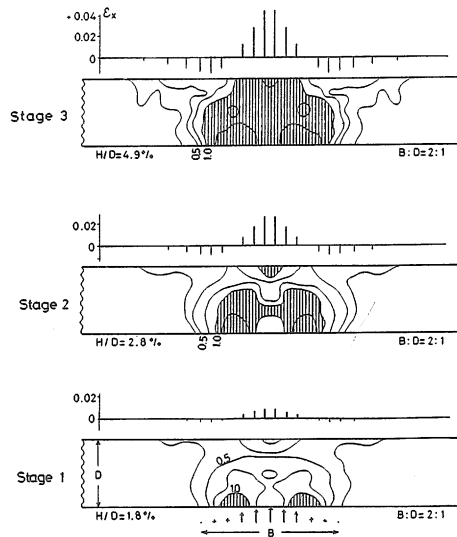dome (W) is almost constant in spite of the increase of H′.

Fig. 19.   Model N-1.   Expansion of yielded zone and change of the surface horizontal
strain (ε_x).   Positive ε_x shows extensile strain.   Contour lines in the model layer
show equivalent stress which is normalized by σ_Y.   The shaded zone shows the
yielded zone where normalized equivalent stress exceeds 1.0.   Arrows are
displacement vector of boundary nodes.

strain near the dome apex is not expanded.

Fig. 20 shows the principal stress distribution in the model crust.   The magnitude
of each stress is changed with increase of deformation, but the distribution pattern of
stresses is scarcely changed.   Maximum tensile stress is mostly horizontal near the
center of the surface dome, but it dips ca. 45° at the side of the dome and is rotated to
almost vertical.

Fig. 19 also shows the relation between the uplift and the expansion of yielded
zone.   This zone is defined as the region where the equivalent stress of each element is
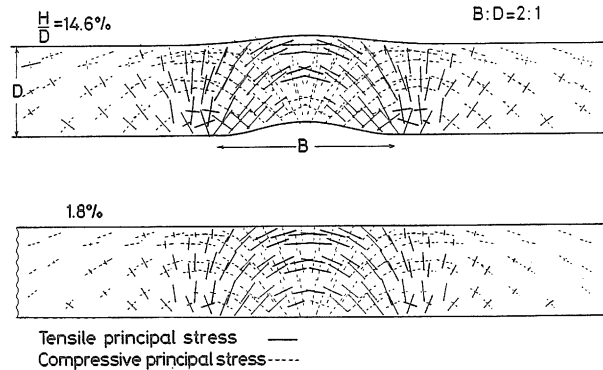
Fig. 20. Model N-1. Principal stress axes in the model crust. The stress distribution of
two stages, H/D=1.8 and 14.6%, are shown. Each stress is illustrated in
logarithmic length by maximum stress.

larger than yield stress $\bar{\sigma}$ exceeds σ_Y. The yielded zone (shaded area in Fig. 19) begins
to expand from the both sides of the basal forced deformation upward. On the other
hand, another yielded zone originates from the center of the surface dome and expands
downward. In this upper zone, equivalent stress gradient increases upward, namely
toward the dome apex. The upper zone soon merges into the yielded zone expanded
from the base.

It cannot be distinguished whether the yielding is caused by tensile, compressive or
shearing stresses, because the Mises' yield criterion is adopted in this model. However,
stress condition of the yielded zone near the center of the surface dome cannot be
identified with that of the deeper yielded zone. The former is produced by horizontal
tensile stresses.

V-2-4-(b). Effect of the depth of a magma reservoir on the surface deformation
(Model N-2A)

Parameter B/D is controlled in Model N-2. Model N-2A tests the effect of
parameter D, namely the depth of a magma reservoir.

Fig. 21 shows the deformation and the horizontal strain of the surface when the
ratio of the surface uplift to the width of the basal deformation (H'/B) is 1.25%.

The width of the dome (W) is enlarged in proportion to the thickness of the layer
(D). Namely, as the magma reservoir exists deeper, the surface dome becomes larger.
Horizontal strains (ε_x) concentrate near the dome apex, and the deeper magma reservoir
produces the smaller and wider distribution of the surface horizontal strains.

V-2-4-(c). Effect of the magnitude of a magma reservoir on the surface deformation
(Model N-2B)

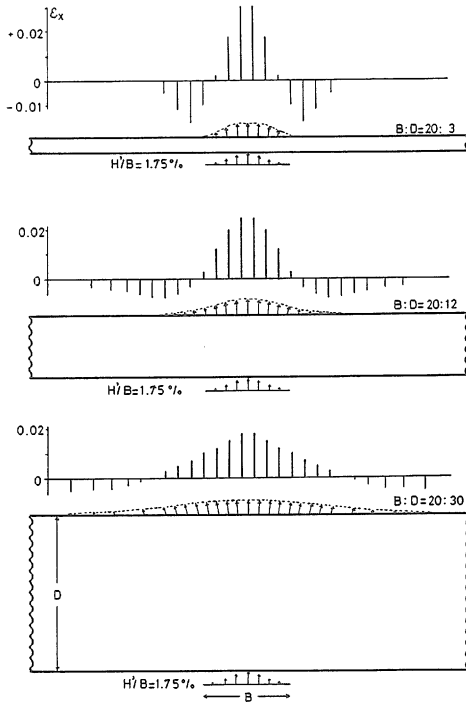Model N-2B tests the effect of the magnitude of basal deformation, parameter B

Fig. 21.   Model N-2A.   Deformation and hori-
zontal strain of the surface.
The positive horizontal strain ϵ_x is
extensile.   The surface displacements
H' are the same in these three cases.
The deformation is illustrated by nodal
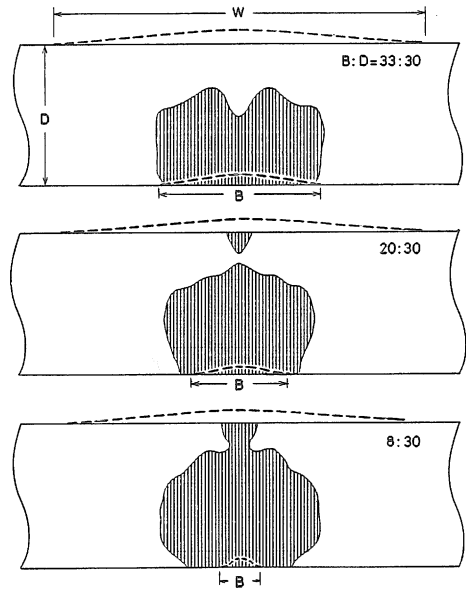displacement vectors ten times as large
as actual length.

Fig. 22.   Model N-2B.   Effect of the magni-
tude of the magma reservoir.
Three cases are compared when these
H'/D equal 1%.   Controlled para-
meter is the width (B) of the basal
deformation.   Shaded   area   is   the
yielded zone.   Note that W is almost
constant in spite of the variable para-
meter B.

that represents the diameter of the magma reservoir.

Fig. 22 shows the resuslts of model N-2B when parameter (B) is changed while
parameter (D) is fixed.   Three cases are compared when these H'/D equal 1%.   It is
worthy to note that the width of the surface dome (W) is scarcely changed in spite of
variation of parameter (B).   The yielded zone spreads more widely with decreasing of
parameter (B).   This may be explained by the evidence that the larger curvature of the
basal deformation produces the wider spreading of the yielded zone.

V-2-4-(d).   Effect of the spacing of magma reservoirs on the surface deformation
(Model N-3)

Model N-3 is planned in order to examine the spacing of magma reservoirs (Fig.

23).   The spacing factor of the two reservoirs (S) is introduced.

The model crust has the same physical parameters as Models N-1 and N-2, and two circular reservoirs are set up separately each other.   The ratio of the surface uplift (H') to the depth of the reservoir (D) is 0.33% in both results.

If the ratio (S/D) is 4/3, the surface dome and the horizontal tensile stress field near the crest are divided into two regions.   However, if the ratio is 2/3, only one surface dome is formed, and a more or less large horizontal tensile stress field is developed near the dome apex.
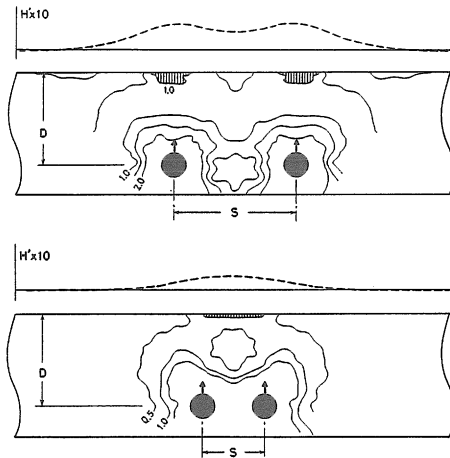

Fig. 23.   Model   N-3.   Model   for   paired
ascending magma reservoirs.
Contour lines: equivalent stress nor-
malized by σ_Y ($\bar{\sigma}/\sigma_Y$), black circle:
magma reservoirs, thick arrow: as-
cending direction, shaded area: yielded
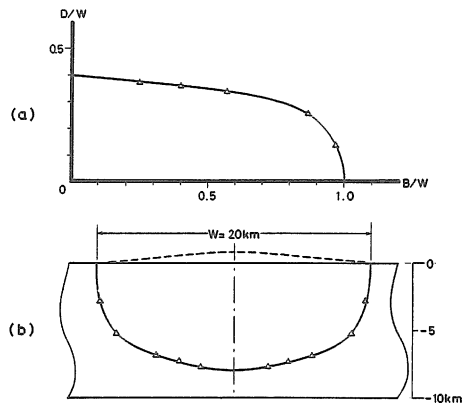zone where horizontal tensile stress is
predominant.

Fig. 24.   Model N-2.   Relation between para-
meters B and D.   (a) Parameters B
and D are normalized by parameter W.
(b) Substitution of the actual diameter
of the surface dome into model para-
meter W.   D-B relation is restricted
within a solid curve.

V-2-5.   Discussion of numerical analyses

Model N-1 reveals that the extent of the horizontal tensile zone at the surface and the diameter of the dome are not related to the amount of uplift (Fig. 18, 19).   They are decided at the earliest stage of deformation within the elastic strain.   Accordingly, the plastic physical parameters also bear no relation to the dome diameter and the horizontal tensile zone.

When parameter D is changed from test to test in Model N-2, the value W responds sensitively (Fig. 21).   The larger D enlarges W, infinitely.   Nevertheless, from the observational facts, the uplift width (W) is limited to ca. 20 km.   Therefore, the parameter D must also be limited.   The relationship between parameters D and B

are given in Fig. 24–a, where both parameters are normalized by the diameter of the surface dome (W). This results shows that neither B nor D can take infinitely large values. When B is zero, the value of D/W is about 0.4. Therefore, the value of D cannot exceed 0.4 times as large as W, even if the boundary force would be just a point movement.

Substituting the mean observed value, 20 km, into the diameter of the dome (W), the maximum value of D takes about 8 km (Fig. 24–b). Even though the maximum observed value in the Motojuku region (FUJITA *et al.*, 1970), 60 km, is substituted into W, the result is $D < 24$ km. If the magma reservosir was situated at a deeper level than 8–24 km, the scale of the dome would exceed 20–60km. Namely, it is concluded that the magma reservoir which produces the surface dome must be situated at a shallow level in the crust.

Model N–3 simulates the paired ascending magma reservoirs. When the initial depth of two reservoirs takes the value 12 km, the reservoir is 3.2 km in diameter, and the distances between two reservoirs are 16 km and 8 km in respective cases of Model N–3. If the distance is 16 km, the surface domes and the horizontal tensile stress fields on the surface are isolated above each reservoir. However, if the distance is 8 km, only one dome is formed, and the horizontal tensile stress fields merge into one around the crest of the dome.

V–3. Scale model Experiments on the Formation of Cauldron

V–3–1. Boundary conditions and experimental apparatus

According to the results of the above finite element analyses, the magma reservoir is inferred to be situated at a depth less than 8 km under the surface, when the dome rise is about 20 km in diameter. In the present scale model experiments the depth of the magma reservoir was taken as 7.5 km. A three-dimensional model which used dry sand and powdered clay to represent the brittle crust was designed.

A rectangular box ($12 \times 45 \times 55$ cm) was used as a container of powdered material. A hole of 1 cm in diameter was made at the bottom of the box, and the shaft having a rigid ball of R cm diameter at the head was passed through this hole (Fig. 25). The shaft was raised by a motor with a constant speed. After adjusting the ball's position to the desired depth D cm, the box was filled with the model material and its surface was evened without compaction. The surface deformation was photographed and sketched from directly above the model, while the amount of uplift and collapse were actually measured.

Since the scale of the model was taken as 1/100,000, the ball's position (D) should be

$$7.5 \ (\text{km})/10^5 = 7.5 \ (\text{cm}) \tag{32}$$

Model S–1 was composed of the ball of 3 cm in diameter and Material I. Material
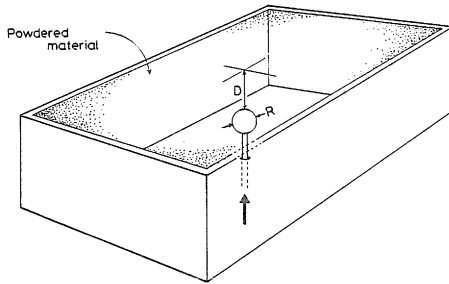
Fig. 25. Model experiment apparatus. Size of a rectangular box is 12×4503655 cm. D: depth of the rigid ball (imitation magma reservoir), R: diameter of the ball.

Table 4. Experimental models (S-series) and controlled parameters.

	D (cm)	R (cm)	Material
Model S-1	7.5	2	I
Model S-2	"	2, 3	I
Model S-3	"	2	II
Model S-4	5 / 10	2 / 4	I
Model S-5	7.5	3	I

I is a mixture of dry sand and powdered clay in the ratio of 3:1, while Material II consists entirely of powdered clay. To examine the effect of the ball's diameter, two cases, R=2 and R=3 cm, were planned (Model S-2). Model S-3 using Material II tested the influence of material. Model S-4 tested the scale effect of the model. Model S-5 was planned in order to test the effect of the subsurface cavity or the contraction of the magma reservoir. The last model was not the ascending reservoir model. These experiments were repeated several times on each model. The combinations of these parameters are shown in Table 4.

V-3-2. Similarity

Conditions of similarity can be obtained by the method of Emori (1985). Because the model reproduces the formation of a collapse structure, one of the important physical laws working on the system is gravity force, which is expressed as

$$F_g = \varrho g l^3 \tag{33}$$

where ϱ, g and l represent density, gravitational acceleration and length, respectively. The force which is caused by the ascending magma reservoir is

$$F = p l^2 \tag{34}$$

where p represents pressure working at the top of the magma reservoir. The internal friction force is given as

$$F_f = \mu \sigma l^2 \tag{35}$$

and the strength against failure is

$$F_c = c l^2 \tag{36}$$

where μ and σ are the internal friction coefficient given by $\mu = \tan \phi$ (cf. equation (45)) and stress, respectively, and c is strength with stress dimension. In such a large

deformation and failure, the effect of elastic force is very small and we can ignore it. Also, no effect of viscosity is recognized, because of brittle failure, and so we need not consider a time scale.

Pi-numbers (dimensionless products) are obtained from equations (33) to (36). Since μ is a dimensionless coefficient,

$$\pi_1 = \mu \tag{37}$$

Then, from (33) and (34) we get

$$\pi_2 = F/F_g = p/\varrho g l \tag{38}$$

or, since the dimension of p and σ is the same,

$$\pi_2 = \sigma/\varrho g l \tag{38'}$$

and from (35) and (36) we get

$$\pi_3 = F_f/F_c = \mu \sigma/c \tag{39}$$

The corresponding pi-numbers between original and model must be equal, so we derive the following expression from equations (37) to (39)

$$\mu = \mu' \tag{40}$$

$$\sigma/\varrho g l = \sigma'/\varrho' g' l' \tag{41}$$

$$\mu \sigma/c = \mu' \sigma'/c' \tag{42}$$

where primes refer to model parameters.

Consequently, when suffix m represents the model ratio of each physical quantity, equations (40) to (42) can be rewritten as

$$\mu_m = \mu'/\mu = 1.0 \tag{43}$$

$$\varrho_m g_m l_m = \sigma_m = c_m \tag{44}$$

With $g_m = 1.0$ and $\mu_m = 0.5$, by taking $l_m = 10^{-5}$, we can obtain the model ratio of the strength as

$$c_m = 5 \times 10^{-6}$$

V-3-3. Physical properties of experimental materials

Cohesive strentgth of rocks is generally of the order of 10^7 to 2×10^7 Pa for sedimentary rocks and 5×10^7 Pa for crystalline rocks, and a friction angle ranges from $10°$ to $60°$ (HANDIN, 1966). When this value is multiplied by the above-mentioned $c_m = 5 \times 10^{-6}$, the strength of model material should be 50 to 250 Pa.

Fig. 26 shows the physical properties of the experimental materials measured by direct shear test. Within the range of $-\sigma < 10^5$ Pa (1.0 bar), linear relations between
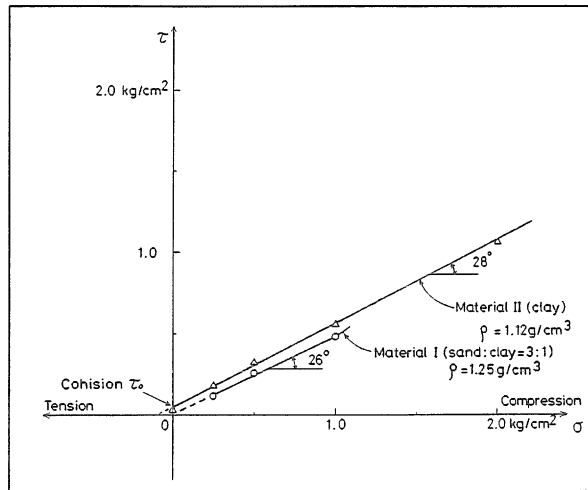
Fig. 26.   Controlled-strain shear tests.

shear and normal stresses were observed.   The relations are expressed by means of Mohr-Coulomb's equation

$$\tau = \tau_0 - \sigma \tan \phi \tag{45}$$

where τ is shear stress, σ is normal stress, τ_0 is cohesive strength, and ϕ is the angle of internal friction.   The friction angle ϕ was about 26° in Material I and 28° in Material II.   The cohesive strength of Material I was about 1.3×10^3 Pa and that of Material II was about 5.2×10^3 Pa.   Although these strength converted into natural scale may be more or less larger than those of rocks, the difference is small.   Material I is more similar to rocks of the crust, because its τ_0 is smaller than Material II.   The friction angles of Materials I and II, which are pi-numbers, are quite similar to rocks.

V-3-4.   Experimental resuslts

V-3-4-(a).   Process of cauldron formation (Model S-1)

The deformation process and fracturing of Model S-1 are illustrated in Fig. 27.

When the imitation magma reservoir ascended more than 10 to 12 mm, the surface began to rise and simultaneously radial fractures started to grow outward from the center of the dome.   Soon after the formation of these radial fractures, short concentric fractures of steep dips were formed and intersected the radial fractures like a letter T. These fractures were distributed concentrically, but each fracture was not arcuated. They grew one after another outward from the center of the dome.   The radial fractures always appeared first and grew outward, which was followed by the growth of the concentric fractures.   Both types of fractures always intersect each other at right angles.   A small block bounded by the radial and concentric fractures was not broken
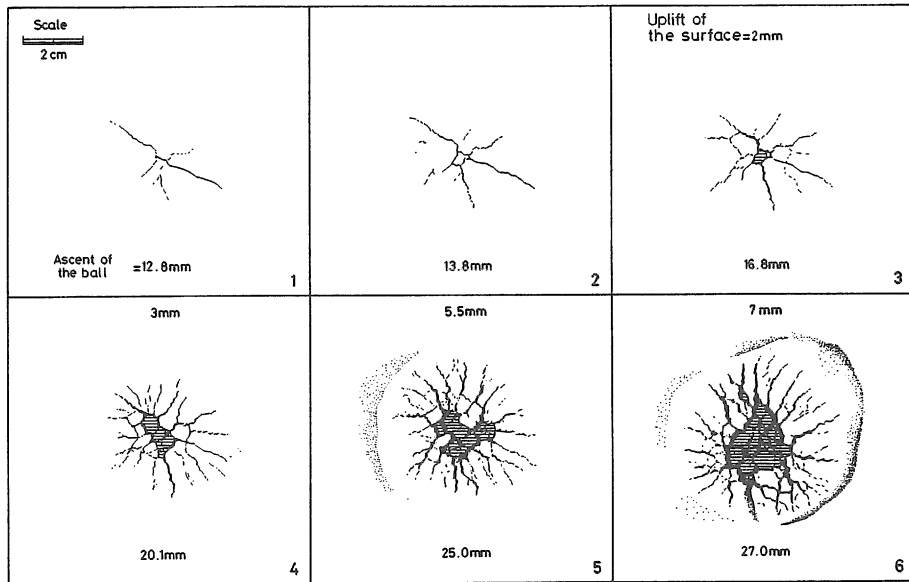
Fig. 27. Model S–1. Cauldron formation caused by domal rise. Material I was used. The surface dome is illustrated by dotted shade, and the shadow zone drown by thin lines shows a collapse part. The maximum displacement of collapse amounted to ca. 2 mm at stage 6.

further and sunk relative to the outside blocks. Thus, collapse structure was formed with a diameter of about one-third of the surface dome. The margin of the collapse basin (caldera) was bounded by nearly vertical fault scarps.

Collapse displacement at the surface was 1–2 mm when the vertical displacement of the dome reached about 7 mm. The displacement of the boundary faults of the basin was probably maximum near the surface. Collapse displacement probably diminishes with depth, according to CURRIE (1956) and SANFORD (1959).

V–3–4–(b). Diameter of an ascending magma reservoir and the surface cauldron (Model S–2)

Fig. 28 shows the result of Model S–2, whose controlled parameter is the diameter of an ascending ball (imitation magma reservoir). The diameter was 2 cm in Model S–2–(a) and 3 cm in Model S–2–(b). The initial positions of two balls were the same.

When the uplift of the surface dome reached ca. 6 mm, the ball of Model (a) was raised 27 mm, and that of Model (b) was raised 15 mm. The diameter of the collapse basin on top of the dome was 18 mm in Model (a) and 28 mm in Model (b). Namely, the size of the collapsed basin was proportional to the diameter of the imitation reservoir whose diameter ranged from 2 to 3 cm.
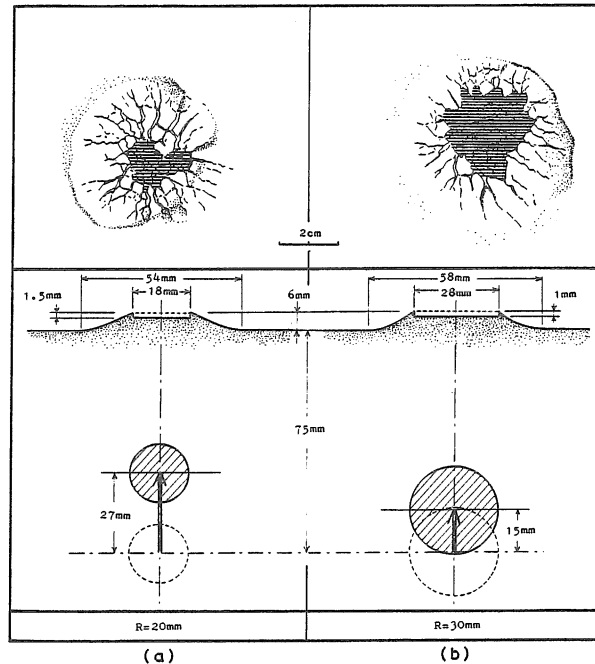
Fig. 28. Model S–2. Effect of the diameter of ascending balls on the diameter of collapse
basin. Upper: plan view, and lower: vertical section. Note that the size of
collapse basin is proportional to the diameter of ascending balls.

V–3–4–(c). Effect of experimental material (Model S–3)

The boundary condition of Model S–3 was similar to that of Model S–1, but
Material II was used (Fig. 29). Material II consisted of powdered clay and had higher
cohesive strength and higher internal friction angle than Material I.

An extension fracture was formed through the center of the surface dome at the
beginning. Then, radial extension fractures extended from the center, but the fractures
were fewer than those of Model S–1. Accordingly, the strain amount was accommo-
dated to the larger opening of each fracture. The top of the surface dome was not
collapsed, because concentric fractures were scarcely formed.

Minor thrust faults were formed at the bottom of the surface dome. The uplift of
the dome and the large opening of fractures caused outward movement of the dome and
radial compression, which probably resulted in the formation of thrusts.

V–3–4–(d). Effect of model size (Model S–4)

Fig. 30 shows Model S–4. Model S–4–(a) and (b) consisted of the same materials,
but the initial boundary condition of model (b) was twice as large as model (a).

The diameter of the surface dome and the collapse basin, the amount of uplift and
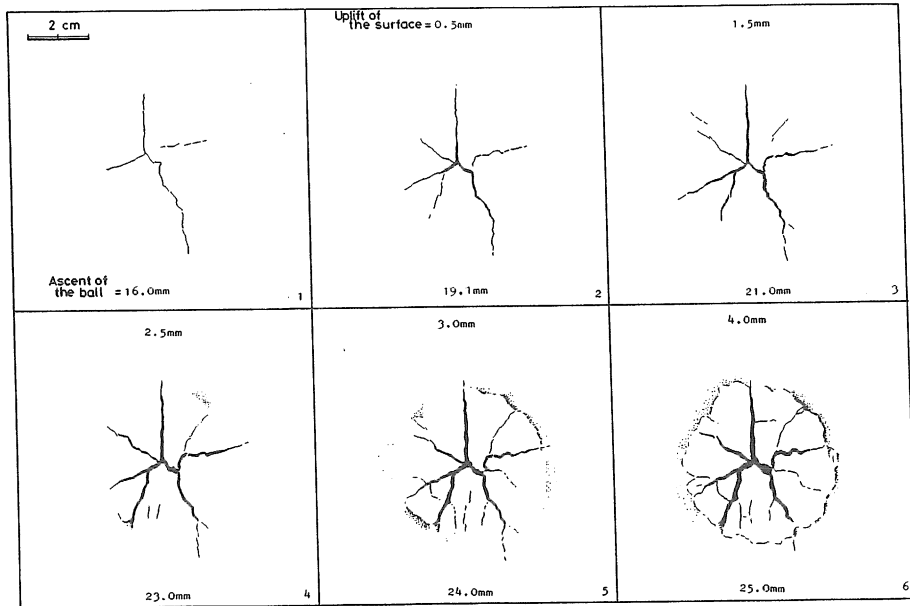
Fig. 29.   Model S–3.   Sketches illustrating the surface deformation and faulting sequence.   Material II
was used.   Compare this result with that of Model S–1, for the boundary conditions of both
experiments are the same.   Note that the caldera collapse did not occur, and radial extension
fractures developed.

Fig. 30.   Model S–4.   The initial boundary condition of the right model (S–4–b) is two
times as large as the sother.

collapse, and the ascending of the imitation reservoir in model (b) were about twice as
large as those in model (a).   The number of fractures of model (b) was more than that
of model (a), but the density of fractures was almost the same.

V–3–4–(e).   Cauldron caused by subsurface cavity (Model S–5)

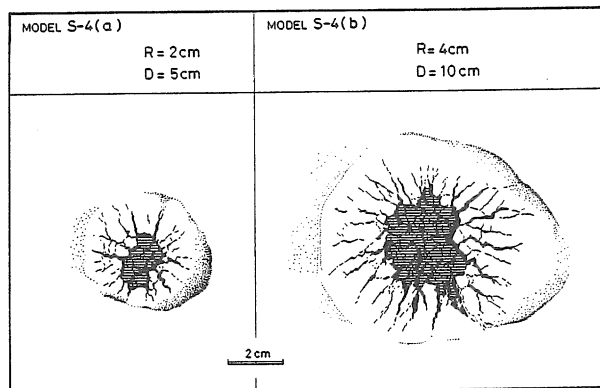Model S–5 was designed in order to investigate the influence of the subsurface collapse of the magma reservoir.   It was composed of Material I holding a ball of dry ice 3 cm in diameter which was set 4 cm under the surface.

Evaporation of the dry ice resulted in collapse of the overburden (Plates II–3, 4). The model surface above the dry ice ball moved downward so that the collapse basin was formed.   The surrounding wall overhung the basin.   Ring fractures were successively formed along the margin of the basin, and the wall peeled off by these fractures. These fractures were seemed to dip outward similarly to the overhanging wall of the basin.   It is important that no radial fractures were formed and neither up- nor downwarping occurred.

VI.   DISCUSSION ON THE MECHANISM OF CAULDRON FORMATION

VI–1.   Formation of Radial and Ring Fractures

The results of Model S–1 are summarized as follows.   When an imitation magma body ascended from the initial position of 7.5 cm below the surface, the surface was elevated to form a dome and simultaneously vertical radial fractures grew outward from the center of the dome.   Vertical short fractures were continuously formed and intersected the radial fractures at right angles.   These short fractures may be regarded as concentric fractures, but each fracture was not arcuated.   No continuous ring fractures were formed.   They grew one after another outward from the center of the dome subsequent to the formation of the radial fractures.   It is noticed that the radial fractures always appeared first, and the concentric fractures followed.   It is also noticed that small blocks bounded by the radial and short fractures were no more broken but sunk relative to the outer blocks.   Thus, a polygonal cauldron (caldera) rimmed by an irregular wall was formed with a diameter of about one-third to one-fourth of the surface dome.   The caldera rim was bounded by nearly vertical fault scarps.   The displacement of the concentric fractures is assumed to be maximum near the surface and probably diminished downward with depth according to the two-dimensional doming model of Currie (1956) and Sanford (1959) (Fig. 31).

On the contrary, the contracting magma body model (S–5) resulted in the formation of ring fractures which dipped outward, but no radial fractures were formed.   The resuslts indicate that the subsurface cavity caused by evacuation of the magma reservoir produces numerous ring fractures which dip outward.   The ring fractures probably produce a bell-jar shaped subsiding block, as expected from the Anderson's two-dimensional analysis (Fig. 32; Anderson, 1936).   The subsurface collapse begins at the roof of the magma reservoir and develops upward.   When the subsurface collapse reaches the surface, a circular cauldron which is surrounded by an outward dipping wall
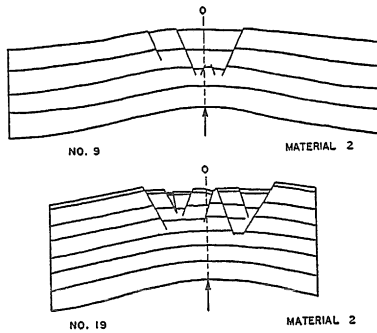
Fig. 31. A model experiment on graben forma-
tion associated with arching of model
crust (SANFORD, 1959). Note that
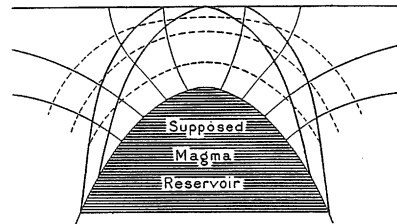fault displacement diminishes down-
ward.

Fig. 32. Stress diagram illustrating supposed
mode of formation of cone-sheets and
ring dikes. Dotted line: tensile prin-
cipal stress, thin line: compressive
principal stress (intruded by cone
sheets), thick line: ring fractures (occu-
pied by ring dikes). (ANDERSON, 1936).

is produced.

Accordingly, the contracting magma body produces a circular cauldron, because
only continuous ring fractures are formed, whereas the ascending magma body leads to
formation of a polygonal cauldron bounded by both radial and concentric fractures.
The faults associated with the polygonal cauldron diminish downward, while those of the
circular cauldron develop dowanward.

The ring fractures formed in Model S–5 are tensile fractures, by which the caldera
wall peels off without shearing slip. These fractures are probably perpendicular to
maximum tensile stress σ_1. Therefore, the contracting magma reservoir in the brittle
crust may cause tensile ring fractures.

ANDERSON (1936) studied cone sheets and ring dikes (Fig. 32). The cone sheets
are characterized by the increase in the amount of the inward dip with depth, and the
ring dikes are vertical and inclined away from the axis of the arc. According to
ANDERSON, cone sheets occupy tension fractures, but PHILLIPS (1974) explained that the
cone sheets occupy shear fractures caused by the pressures resulting from the rapid
expansion of a retro-boiling magma. ROBSON and BARR (1964) also concluded that the
cone sheets occupy shear fractures. These analyses were based on a two-dimensional
model. However, model experiments of three-dimension performed by the author
revealed that no continuous cone fractures were produced. The discontinuous concen-
tric fractures in Model S–1 may represent cone fractures. Field observations also show
that cone sheets are usually short and not continuous (RICHEY, 1961).

ANDERSON (1936) and PHILLIPS (1974) pointed out that ring dike intrusions into ring
fractures occurred under reduced magma pressure or by subsidence of a magma body.
ROBSON and BARR (1964) argued that tensile ring or radial fractures are produced just
above a magma body. They suggested that ring fractures dip outward under low
magma pressure whereas they dip vertically under high magma pressure. ROBERTS

(1970) mentioned that some inward-dipping ring dikes occupy tensile fractures formed under excess magma presure, whereas other outward-dipping ring dikes fill shear fractures formed under reduced magma pressure. BILLINGS (1943), according to CLOUGH et al. (1909), inferred that a magma body pushed on its roof like a punch so that vertical ring fractures formed above the magma body. KATSUI and KOMURO (1984) recognized the mechanical origin of the ring fractures on the summit of Komagatake Volcano of Hokkaido, north Japan, as the withdrawal of a magma column or the local large compaction of a new pumice cone piled on the summit. The Hawaiian type calderas, which show circular outlines, are formed after voluminous outpouring of basic lavas (WILLIAMS and McBIRNEY, 1979). Accordingly, most workers considered that vertical to outward-dipping ring fractures are formed under reduced magma pressure or subsidence of the magma body. On the other hand, inward-dipping to vertical ring fractures were considered to originate by excess pressure of the magmatic body itself. BILLINGS' opinion is unique, but the stiffness of magma may not be so high to perforate the crust.

Anderson, BILLINGS and PHILLIPS considered that ring fractures were produced by shearing, but ROBSON and BARR regarded these fractures as tensile in origin. ROBERTS concluded that some fractures are shear and others are tensile fractures. However, the difference between the shearing and tensile types of fracturing is not important. These two types are mutually transformable, because the shearing angle is a function of the Mohr envelope, which is decided by the physical property of material. That is, under the same stress condition, if the shearing angle is very small, extensile fractures develop; on the other hand, if it is large, shearing fractures become predominant. Near the earth's surface, since maximum shearing stress is small and maximum tensile principal stress indicates tension, the shearing angle tends to take a small value.

ROBSON and BARR (1964) regarded radial dikes as due to tensile failure, while PHILLIPS (1974) thought the fractures intruded by radial dikes to be simple hydraulic tension fractures which were formed periodically during the upwelling of magma. However, they did not discuss which fractures were formed first. KOIDE and BHAT-TACHARJI (1975) pointed out in their three-dimensional analyses that radial tension fractures develop more widely than concentric tension fractures by excess pressure of the magma body which is placed at a fixed level, and is nearly spherical or vertically elongated ellipsoidal in shape (Fig. 33). They did not discuss the priority of radial and concentric fractures, because their model was based on elastic analyses. Although a central ring fracture zone is produced in their model, continuous concentric fractures may not be formed as inferred from the author's Model S–5. Moreover, they did not discuss the effect of the earth's surface. In their model, stress magnitude monotonously decreases upward from the top of the magma body, but KOMURO et al. (1977) revealed that horizontal tensile stress concentrates near the center of the surface dome and increases upward.

WITHJACK and SCHEINER (1982) demonstrated that radial fractures were always
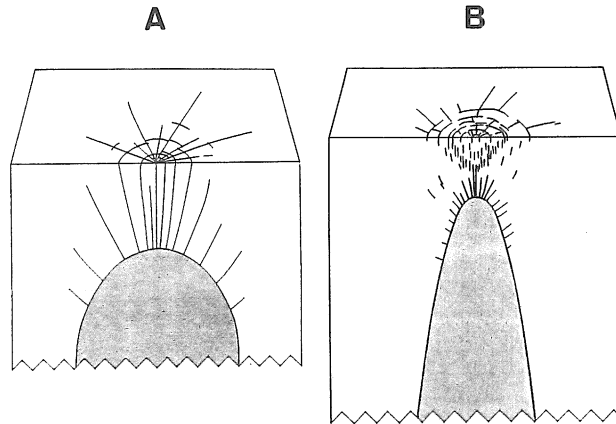
A   B

Fig. 33. Possible fracture patterns around spherical and elongated magma reservoirs formed by magma pressure higher than lithostatic stress (KOIDE and BHATTACHAR-JI, 1975). Fracture pattern is controlled by the shape of magma body. If the magma reservoir is spherical, radial fractures cut concentric ones (A). If it is vertically elongated, en echelon concentric tension fractures develop (B).

widely distributed on the swelling dome of their clay models. PARKER and McDOWELL (1955) performed model experiments of salt dome dynamics with an overburden of barite and a buoyant asphalt layer, and showed that radial fractures were always dominant, and a polygonal (not circular) cauldron was formed at the center of the dome. This model had the ascending magma body with a variable shape and low stiffness. Their results are concordant with the model of the ascending rigid ball (Model S-1). Namely, stiffness and shape of the ascending magma body probably did not control the surface deformation associated with the cauldron, because this type of cauldron is the result of surface doming.

When the model material with a higher cohesion than Model S-1 was used, no concentric fractures were produced but only radial fractures developed (Model S-3). Accordingly, the magma body ascending in the more highly cohesive crust, for example in a cratonic environment, would cause central eruption or radial fissure eruption on the dome before a ring cauldron might be formed by the evacuation of magma.

VI-2. Fracture Systems of the Experimental Resuslts in Comparison with Observed Evidence

The radial and concentric fractures formed by doming mutually intersect at right angles. The small blocks bounded by the fractures of these two fracture systems are the minimum unit of collapse. The outline of the collapse basin shows an irregular polygonal shape in plan, because the collapsed part is composed of an assemblage of such small blocks. This shape is concordant with the geological facts. The Sunago-hara and Honna cauldrons show irregular outlines with complicate faults.
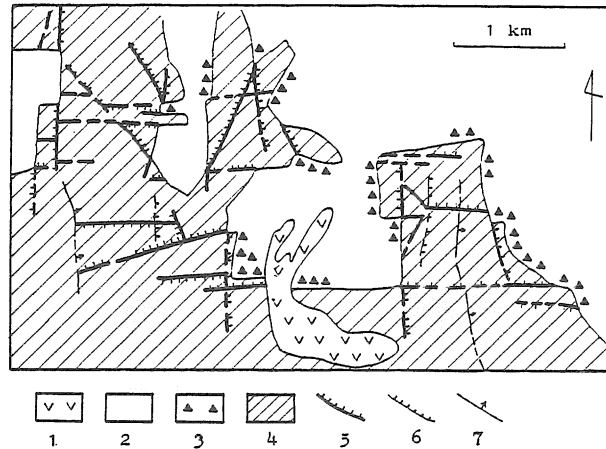
Fig. 34.   Faults near the southwestern margin of the Motojuku cauldron (simplified from
FUJITA and FUKAZAWA, 1979).
1: dike, 2: cauldron fills, 3: sedimentary breccia, 4: basement rocks, 5: normal
fault, 6: lateral fault, 7: reverse fault.   Note the relation between the unconform-
able margin of the cauldron and faults.

FUJITA and FUKAZAWA (1979) studied the fault system observed in the southwestern
margin of the Motojuku cauldron, and found normal, reverse and strike-slip faults in the
basement (Fig. 34).   It is noted that these faults are not curved.   Neither ring fractures
nor arcuate faults were observed.   They concluded that the cauldron collapsed along
the normal faults, because these faults conformed to the complicated cauldron rim which
is not a fault contact, but an unconformity.   The unconformity, steeply dipping toward
the cauldron bottom, represents an ancient fault scarp which has been preserved by
successive deposition of intracauldron beds without erosion.

On the other hand, radial fractures are formed all over the dome in the experi-
ments, whereas such fractures have not been scarcely confirmed in the field survey.
This disagreement may be explained by the incomplete similarity of model to prototype.
For instance, the strength of the model material should have been taken at a lower
value.   Alternatively, most of the radial fractures may not be noticed in field survey,
because these fractures have no vertical displacement so that they are difficult to be
found.

Whether or not radial fractures can be discovered by field survey in future is
important for the similarity of the model.   Because the radial fractures are extension
fractures, they would be the optimum feeding routes of magma, and they may be
reserved as dikes, or clastic dikes.   Accordingly, further field survey around cauldrons
should give attention not only to the fracture systems but also to the arrangement and
direction of these dikes.   YOSHITANI and YAMAUCHI (1981) reported some remarkable
breccia dikes which were formed in the earliest stage of cauldron were found in the

basement around the cauldron. These breccias were regarded as sediments of talus origin. Namely, open fractures around the cauldron were probably filled with the sedimentary breccia of talus origin. In the western Mediterranean, Corsica, "an initial doming of the crust, attributed to excess pressure in the underlying magmatic chamber, causes an essentially radial fracturing (more rarely concentric with strong inward dip). The fracturing allows the emplacement of feeder dykes for pyroclastic eruptions, ignimbritic flow and the formation of domes. These pre-caldera formations are preserved outside the caldera limits when not destroyed by erosion." (BONIN, 1986). Both examples support the presence of extensile open fractures caused by doming.

VI-3.   Parameters Controlling Collapse Caused by Doming of the Crust

Because the concentric fractures appeared in the early stage of the cauldron formation are of extension, they are inferred to be formed under tensile stress. Accordingly, the collapse resulting from these fractures may occur within a tensile stress region.   In Model N-1 of finite element analysis (Fig. 21), horizontal extensile strain of the surface is concentrated near the crest of the dome. This extensile domain is estimated to coincide with the extent of a collapse caldera. The caldera may not to extend beyond this domain, because the extent of the extensile domain depends on the depth of basal deformation rather than the amount of uplift, as clearly shown in Model N-2 (Fig. 24). When the tensile stress within the domain exceeds the strength of material, concentric faults develop to form cauldron. However, the deeper reservoir produces a smaller amount of horizontal tensile strain at the surface (Model N-2A). Accordingly, the displacement of collapse is inferred to decrease with a depth of the reservoir.

The yielded zone shown in numerical models is characterized by plastic strain, which is regarded as permanent dislocation of particles, for example, microfractures in rock. Faults in the earth's crust are also regarded as permanent dislocation. Accordingly, the yielded zone may represent the fault zone. The yielded zone of the numerical model is divided into three types; the first and the second are characterized by the horizontal tensile and compressive stresses near the surface, respectively, and the third is characterized by the two compressive stresses just above the magma. Though Mises' criterion cannot express this difference, the principal stress distribution (Fig. 20) shows that the horizontal tension concentrates near the crest of the surface dome. The gradient of equivalent stress in this tensile domain(Fig. 19) shows that higher stress concentrates near the surface. Namely, if many faults are formed in this tensile yielded zone, these displacements may increase upward, and these faults diminish downward. The results of previous experiments of two-dimensional model (CURRIE, 1956; SANFORD, 1959) also show that the marginal or inside faults of a graben develop near the center of the surface dome and diminish downward. The strain also increases toward the crest on the surface. Accordingly, the floor of the caldera may be composed of step-like

faults down to the center.

In Model S–2, using highly cohesive material (Material II), concentric fractures were little deverloped, so that the cauldron was not produced. Radial fractures were also fewer in Model S–2 than in Model S–1. It is cosnsidered, therefore, that the difference cohesion of the eath's crust affects the density of fractures, which consequently determines whether the collapse structure would be formed or not.

It can be concluded that the geometric parameters, such as the width of uplift and the potential domain of collapse, are determined by the boundary conditions. The actual collapse is caused within the extensile domain near the crest of the surface dome, when the strength of the crust is small.

If two magma reservoirs separately ascend, the surface extensile domain may be formed apart (Model N–3). In this case, two separated cauldrons are caused under low cohesion of the crust.

VI–4. Diameter of Cauldron

According to the results of Model S–3, the diameter of the cauldron seems to be a function of the size of the imitation magma reservoir, at least within the range of 2 to 3 cm in diameter. These values correspond to 2 to 3 km diameter in natural scale. The size of the reservoir may determine the shape and curvature of the surface dome, if the reservoir is situated at a shallow position of the crust. KOIDE and BHATTACHARJI (1975) also showed that the diameter of a concentric fracture zone is almost the same as that of the reservoir regardless of the shape of the reservoir, though they did not take the effect of the earth's surface into consideration.

BONIN (1986) reviewed analytical works of ANDERSON (1936), ROBSON and BARR (1964), PHILLIPS (1974), BROUL and KATTERFELD (1977) etc., and concluded that "... in all cases the same relationship $d=2R$ applies", where, d is the depth of the apex of the magma reservoir with excess pressure, and R is the caldera radius. He said, "this links the diameter of the caldera to the depth of the magmatic chamber". According to him, if the cauldron is 5 km in diameter, the depth of the apex of the reservoir is about 10 km and its size has no relation to the cauldron radius. Model N–2A in this paper also shows that the increase in depth of the apex of the reservoir causes expansion of the extensile horizontal strain region at the surface. Accordingly, the results of the numerical experiments are concordant with BONIN's conclusion despite the different boundary condition. However, if the top of the reservoir is shallow, its size would control the caldera radius.

VI–5. Magnitude of Collapse

The collapse displacement of Model S–1 was 1 to 2 mm, when the uplift of the dome reached 7 mm. These values correspond to 100 to 200 m and 700 m in natural

scale, respectively.   The thickness of the bed abutting on the steeply dipping surface of unconformity at the cauldron margin is 150–200 m.   This value may represent a part of the vertical displacement of collapse, because the steeply dipping surface of unconformity was produced by faulting.   Therefore, the vertical displacements obtained from the experiments are concordant with the observational data, though the experimental values may be slightly less.   The collapse volume, 5 km in diameter by 200 m in displacement, may not be explained by the subsurface collapse above the reservoir but by this surface collapse.   The collapse is inferred to be restricted in a shallow part of the earth's crust, because the vertical displacement of the faults producing collapse is maximum near the surface and gradually decreases downward (see section VI–2).   Namely, the "volume deficit" problem of the cauldron can be ascribed to the surface horizontal extension due to the domal rise.

VI–6.   Comparative Discussion of Some Cauldrons Associated with Ring Fractures

According to WILLIAMS and McBIRNEY (1979), "A caldera is a large volcanic collapse depression, more or less circular or cirquelike in form".   Krakatoan type calderas are "formed by the foundering of the tops of large composite volcanoes following explosive eruptions of siliceous pumice".   However, ring fractures are not essential to the formation of Krakatoan caldera because the collapse is chaotic.

OIDE (1968) suggested that most of the Japanese Krakatoan calderas show polygonal outlines, because of the restriction of the regional tectonic trend.   Therefore, the circular outline and the ring faults are not always confirmed.   YOKOYAMA (1963, 1969) opposed the concept of the collapse origin of Krakatoan calderas.   He pointed out that gravity anomaly around calderas does not demonstrate the boundary faults along the caldera rim and concluded that the calderas are depressions enlarged by catastrophic eruptions.   He also carried out a gravity survey around the Motojuku cauldron and concluded that any noticeable gravity anomaly characteristic of caldera structure was not found (YOKOYAMA, 1974).   However, in this case, boundary faults can be observed (Fig. 34).

SMITH and BAILEY (1968) divided collapse calderas into two types, (1) Kilauea type and (2) Krakatoan type.   Kilauea type calderas are considered to be the best examples of the author's Model S–5, which were formed along ring fractures after voluminous outpouring of basic lavas.   The Krakatoan type was subdivided into (2a) typical Krakatoan type calderas and (2b) those in which a coherent crustal block subsided along ring fractures.   They mentioned that most of the world's calderas belong to group (2), while "Williams' 'Glen Coe type' structure, which included all the classical cauldron subsidences and ring complexes" was incorporated into group (2b), although YOKOYAMA (1958) grouped the Glencoe type calderas into type (1).   SMITH and BAILEY regarded the difference between Glen Coe and Krakatoan type structures as the level of denudation.   They said, "the Glen Coe and Krakatoan denudation sequences are

probably very different, yet both of these structures seem to owe their major subsidence to a common cause". They thought much of pyroclastic eruption preceding these caldera formation as the trigger of subsidence.

Subgroup (2b) is defined as the Valles type caldera. According to SMITH and BAILEY (1968), it is outlined as follows: (i) regional tumescence and generation of ring fractures; (ii) caldera forming eruptions of ash and pumice from the ring fracture system; (iii) caldera collapse. A central oval block, 8 by 10 miles in diameter and bounded by the inner ring fracture, subsided to a great depth, from 2000 to 3000 feet, as an almost intact crustal block — formation of a caldera lake, eruption and deposition of rhyolite lavas and pyroclastics, and deposition of lake bed, talus and landslides from caldera walls; (iv) pre-resurgence volcanism and sedimentation; (v) resurgent doming; (vi) major ring-fracture volcanism — eruption of late rhyolite formed a discontinuous ring of rhyolite pyroclastic cones, domes and flows. This type calderas are characterized by regional tumescence before ring fracture eruption, subsidence of coherent crustal block along the ring fracture and resurgent doming.

According to SMITH and BAILEY, the best evidence of regional tumescence is the simultaneously produced cauldron ring fracture system itself. They regarded the cause of tumescence as the expanding magma.

SMITH and BAILEY (1968) concluded that the collapse of the Valles caldera was caused during and mainly after the major eruptions, because the thickness of tuff accumulated at the eruption stage of a major ash-flow is no greater inside the caldera than outside. STEVEN and RATTÉ (1965) suggested that the Creede caldera may have subsided concurrently with volcanic eruptions. LEUDKE and BURBANK (1966) mentioned that the San Juan volcanic depression was produced after the first cycle eruption and the pyroclastic rocks and lava flows of the subsequent eruptions accumulated within the depression. This later eruption resulted in the formation of Silverton and Lake City cauldrons. LIMPAN (1976) illustrated thick intracaldera tuff and thin outflow tuff of the Lake City caldera. CHRISTIANSEN et al. (1965) pointed out that the Timber Mountain caldera was formed by collapse during and after the eruption of a large volume of ash-flow tuff. They also mentioned that a broad domal swell developed before the climactic eruption. Accordingly, these cauldrons "represent either filling of an already formed depression or filling that is concurrent with subsidence" (SMITH and BAILEY, 1968). These facts suggest that some of the Valles type calderas may have collapsed before the main eruption, such as the Motojuku-type cauldron.

According to SMITH and BAILEY (1968), "the dominant mechanism leading to cauldron formation is doming with the formation of concentric (and radial) fractures, along which subsequent collapse occurs". However, fractures caused by doming are not arcuated, and continuous ring fractures cannot be produced by doming (Model S–1). Accordingly, it is expected that ring fractures of the Valles-type cauldron may not have been produced during the doming but after the main eruption.

SELF et al. (1986) pointed out that the Valles caldera rim was nearly coincident in

position with the previous Toledo ring fracture and caldera.   Moreover, they concluded that initial Plinian falls and early pyroclastic flows emanated from central vents.   They pointed out that there was no strong evidence to suggest a transition to ring fracture eruption.   Namely, the Valles ring fracture, estimated by the ring arrangement of post caldera rhyolite domes, would have been formed after the main eruption, if it had occurred.

Some Tertiary examples of the Valles type cauldron have recently been reported in Japan (KOUDA and KOIDE, 1978; MURAKAMI et al., 1982; AWATA, 1984; YOSHIDA, 1984). Ring fractures were found in some cauldrons.   However, the resurgent dome which characterizes the later stage of this type cauldron is not always observed in these Japanese 'Valles' type cauldrons.   Since these cauldrons are about 10 km or less in diameter, magma reservoirs may have solidified before resurgent doming (MARSH, 1984).

The primary collapse of the Motojuku cauldron was produced by perpendicularly intersecting normal faults.   These normal faults may be similar to radial and concentric fractures of Model S-1.   On the contrary, the secondary collapse of the Motojuku cauldron, which is a ring flexure smaller in diameter than the primary collapse, may have been caused by ring fractures.   It shows more or less a circular outline with a downdropped central block after the voluminous outpouring of lava.   No local uplift occurred just before or after the secondary collapse, since the stratigraphic gap is not observed in the cauldron.   These facts suggest that the results of Model S-5 can be accommodated to the secondary collapse of the Motojuku cauldron.   The secondary Motojuku cauldron is a ring flexure lowered after the voluminous outpouring of lava. This sequence is similar to that of cauldron subsidence.   DALY (1933) concluded that the cauldron subsidences, e.g. Glencoe, Ben Nevis and Etive, were characterized by foundering of blocks surrounded by ring fractures (ring-fracture stoping), rather than by sinking of fragments (piecemeal stoping).

According to BILLINGS (1943), if the pressure in the magma reservoir decreases, the tension fractures parallel to the contact of the reservoir are produced in the surrounding rocks.   The block bounded by such fractures, which have the shape of a paraboloid and convex upward, founders into the reservoir.   This type of subsidence was named underground cauldron subsidence (BILLINGS, 1943).   On the other hand, he defined another type of cauldron as surface cauldron subsidence.   It is characterized by the vertical ring fracture which maintains its steep dip up to the earth's surface and by volcanic rocks derived from the underlying reservoir.   However, density difference between magma and the roof rocks may be too small to cause fracturing and foundering of the roof.   Accordingly, evacuation of magma caused by surface volcanism might have been associated with the underground cauldron subsidence.

Many collapse calderas and surface cauldron subsidences have been considered to be produced after catastrophic eruption of ash or outpouring of lava.

Although the secondary collapse has not been observed in other cauldrons of the

Motojuku-type, some cauldrons mainly of Paleogene to Neogene age in western Japan are characterized by vertical to outward-dipping ring faults (MURAKAMI, 1973; MURAKA-MI et al., 1982; MASUDA R.G., 1982; YOSHIDA, 1984).   These cauldrons downdropped during or after major eruptions, because volcaniclastic and volcanic rocks filling the cauldron are cut by ring faults and/or folded by ring flexures.   Some cauldrons show the basin structure with the dip abruptly increasing near the margin.   Accordingly, the subsiding mechanism of these cauldrons seems to be similar to that of ring complexes. Namely, the roof of the magma body may have collapsed along the bell-jar shaped ring fractures produced by the evacuation of magma.

Plutonic bodies and many dikes intruded into the Motojuku cauldron mainly after the secondary collapse of ring cauldron type, though such intrusions are rarely observed in other cauldrons of Motojuku-type in Japan.   However, other ring cauldrons tend to yield the intrusion of plutonic rocks (RICHEY, 1961; MURAKAMI, 1973; MURAKAMI et al., 1982; YOSHIDA, 1984).   Accordingly, plutonism in cauldrons may be closely related to ring fracturing.

Model S–1 and the previous experiments (SANFORD, 1959; CURRIE, 1956) suggest that with ascending of the magma reservoir there is an increase in displacement of boundary faults of the cauldron with a polygonal shape in plan, and that such faults are not deeply rooted to the magma reservoir so that the magma body is not collapsed. For example, the faults of the Motojuku-type cauldron may be restricted to a shallow crustal level.   On the contrary, Model S–5 shows that the ring cauldron developed upward from the magma body after initial collapse of the roof due to evacuation of magma.   Thus, the ring cauldron may cause collapse of the magma body, which led to the upward moving magma successively replacing the collapsed roof rocks.   When the displaced magma reaches a certain level of the eath's crust through ring fractures, it may be emplaced as ring or central plutonic intrusions.

Fig. 35 shows a schematic model for the development of cauldrons: (A) doming may yield only radial fractures in the case of high cohesion of the crust.   (A′) the surface polygonal cauldron.   Most of the Motojuku-type cauldrons may be included in this stage.   (B) subsurface ring fracturing.   If this ring cauldron reaches the floor of the pre-existing cauldron, a ring flexure may develop.   Minor plutonic intrustions occur. The secondary Motojuku cauldron is considered to be of this type.   Accordingly, the Motojuku cauldron involves the sequential stages (A′) to (B).   If the crust had higher cohesion, a central volcano with or without radial fissures, instead of the primary polygonal cauldron, would be formed with crustal doming.   If the central eruption is large in magnitude, it may result in the formation of a circular cauldron (type (A) to (B)).   In this case, the cauldron may be formed not before but after the eruption from the central vent or radial fissures.   Kilauea caldera is a cauldron of this type, and other circular collapse calderas, e.g. Toledo and Valles calderas (SELF et al., 1986), may be classified in this type.

A
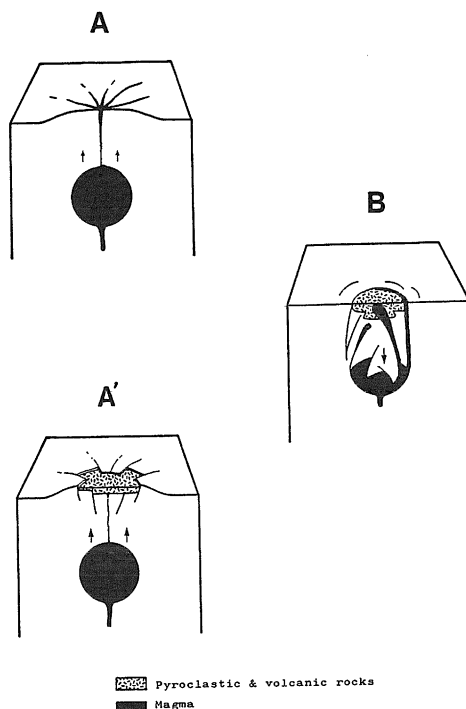
B

A'

Pyroclastic & volcanic rocks
Magma

Fig. 35. Schematic profiles of cauldrons. (A) Radial fractures produced by doming of the cohesive crust. Cauldron is not formed, because no concentric fractures are developed. (A') Polygonal cauldron associated with a domal rise of the lower cohesive crust. Boundary concentric faults diminish downward, so that the cauldron develops near the surface. Fracturing and caldera collapse trigger off eruption. (B) Ring cauldron associated with subsurface cavity. Evacuation of magma causes the subsidence of cauldron. Boundary ring fractures develop upward and cut the previously effused materials. The collapse of the magma body causes many plutonic intrusions toward the surface.

VII. CONCLUSION

1. Two upper Miocen cauldrons were found in the Aizu district, Fukushima Prefecture, Northeast Japan. They are characterized by irregular-polygonal outlines, vertical faults in the basement, unconformity surface steeply dipping into the cauldrons, marginal sedimentary breccias, *etc*. Each cauldron is about 5 km in diameter with vertical displacement 150–200 m. Both cauldrons are regarded as the Motojuku type cauldrons.

2. A domal rise is estimated to have emerged before the cauldron formation. It may be produced by ascent of a magma reservoir. The size of the dome is estimated to be 15–25 km in diameter with uplift ca. 400 m.

3. The following sequence of the formation of the Sunagohara cauldron is concluded: (i) A domal rise was caused by the ascent of the magma reservoir. (ii) A complicated polygonal caldera was produced due to surface doming. Sedimentary breccias of talus origin were deposited along the caldera rim. (iii) Volcanic activity began in the cauldron due to the emission of magma through the many fractures formed during the doming and collapse. Talus accumulations were taken place concurrently with the eruptions. Acidic pyroclastics, which were finer upward, filled the cauldron, and perlite lavas flowed out mainly in the last stage. This process agrees with that of the primary Motojuku cauldron. However, the secondary collapse and the intrusion of dikes and plutonic rocks observed in the Motojuku cauldron are not found in the Sunagohara cauldron.

4. Numerical analyses revealed the following results. The diameter of the surface dome does not extend beyond the limit of the rising dome. A horizontal tensile stress zone which is assumed to be the potential collapse zone is formed near the center of the surface dome. The size of this zone depends largely on the reservoir position. The diameter of the surface dome is sensitively controlled by the depth of the reservoir.

5. If the domal rise is ca. 20 km in diameter, the magma reservoir must be situated less than about 8 km in depth.

6. The results of scale model experiments using powdered clay and sand are as follows. Radial and concentric fractures were formed on the top of the domal uplift, and the inside of the concentric fractures subsided. An irregular polygonal basin of 2–3 cm across with a vertical displakcement of about 2 mm, was produced. The diameter of the dome and the extent of fractures are controlled by the depth of the ascending reservoir. Fracture density is controlled by physical properties of material. The diameter of the caldera may depend on the diameter of the ascending reservoir. A subsurface cavity produced ring-reverse fractures and caused a circular cauldron. No radial fractures were formed in this case.

7. The polygonal cauldron is produced by the domal rise of the surface. Its boundary faults diminishes downward. On the other hand, the circular cauldron is produced by the subsurface cavity. The displacement of the boundary faults increases upward.

8. If collapse calderas are produced by contraction or subsurface cavity of the reservoir after large eruptions, ring fractures must be formed. This mechanism can be concordantly applied to the conventional cauldron subsidence and caldera collapse. If the domal rise due to the ascending of the magma reservoir results in the formation of cauldron, a polygonal shaped caldera must be formed. The polygonal cauldron subsidence is preceded by the domal rise.

9. Subsidence of the polygonal cauldron is accommodated with the horizontal extension on the rising dome apex, but circular cauldron subsidence is triggered off by large evacuation of magma in terms of large pyroclastic flow, voluminous outpouring of lavas, *etc.*

Acknowledgements

References

ANDERSON, E. M., 1936. The dynamics of the formation of cone sheets, ring-dykes, and cauldron subsidences. *Proc. Roy. Soc. Edinburgh*, **56**, 128–163.

AWATA, Y., 1984. Late Miocene-Pliocene calderas in Northeast Japan. *Bull. Geol. Survey Jpn.*, **35**, 439–440 (in Japanese).

BILLINGS, M. P., 1943. Ring-dikes and their origin. *Trans. N.Y. Acad. Sci.*, Ser. 2, **5**, 131–144.

BONIN, B., 1986. Ring Complex, Granites and Anorogenic Magmatism. North Oxford Academic, London, 188 pp.

BROUL, J. J. and KATTERFELD, G. N., 1977. Genesis of ring- and radial-concentric structures of planets (from a rock mechanic's point of view). *Modern Geol.*, **6**, 101–115.

CHRISTIANSEN, R. L., LIPMAN, P. W., ORKILD, P. P. and BYERS, F. M., Jr., 1965. Structure of the Timber Mountain resurgent dome, Nevada, and its relation to Basin and Range structure. *U.S.G.S. Prof. Paper*, 525-B, B43–B48.

CLOOS, H., 1939. Hebung-Spaltung-Vulkanismus. *Geologische Rundschau*, **30**, 404–525.

CLOUGH, C. T., MAUFE, H. B. and BAILEY, E. B., 1909. The cauldron-subsidence of Glen Coe, and the associated igneous phenomena. *Quart. J. Geol. Soc. London*, **65**, 611–676.

CURRIE, J. B., 1956. Role of concurrent deposition and deformation of sediments in development of salt-dome graben structures. *Bull. Am. Assoc. Pet. Geol.*, **40**, 1–16.

DALY, R. A., 1933. Igneous Rocks and the Depths of the Earth. McGraw Hill, N.Y., 598 pp.

EATON, G. P., CHRISTIANSEN, R. L., IYER, H. M., PITT, A. M., MABERY, D. R., BLANK, H. R. JR., ZIETZ, I. and GETTINGS, M. E., 1975. Magma beneath Yellowstone National Park. *Science*, **188**, 787–796.

EMORI, I., 1985. Scale Models in Engineering. Giho-do, Tokyo, 272 pp. (in Japanese).

FUJITA, Y., 1967. Geologic problems on the generation of the Green Tuff movement. *J. Geol. Soc. Jpn.*, **73**, 106 (in Japanese).

———, KAWAKITA, T. and ARAI, T., 1970. Tectogenesis in the formative process of the Motojuku Green Tuff beds—with special reference to depression and igneous activity. *Monogr. Assoc. Geol. Collab. Jpn.*, 16, 81–95 (in Japanese).

———, 1972. The law of generation and development of the Green Tuff orogenesis. *Pacific Geol.*, **5**, 89–116.

———, HAGIWARA, S., SUZUKI, K., YASHIMA, R. and MANABE, K., 1974. A geotectonic study of the tectonic field in the latest Miocene in the Aizu district, Japan. *Marine Sci.*, **6**, 24–29 (in Japanese).

GORSHKOV, G. S., 1959. On some theoretical problems of volcanology. *Bull. Volcanol.*, **19**, 103–113.

HAYAKAWA, N. et al., 1972. Report on the regional geology of the Nishi-Aizu district. MITI of Japan, 27 pp. (in Japanese).

————, et al., 1972. Report on the regional geology of the Higashi-Aizu district. MITI of Japan, 35 pp. (in Japanese).

HANDIN, J., 1966. Strength and ductility. *Geol. Soc. Am. Mem.*, **97**, 223–289.

HIRABAYASHI, T., 1966. Internal structure of black-ore deposit of the Yokota Mine. *Mining Geol.*, **16**, 76–77.

JAEGER, J. C., 1956. Elasticity, Fracture and Flow with Engineering and Geological Application. Methuen, London, 268 pp.

KATSUI, Y. and KOMURO, H., 1984. Formation of fractures in Komagatake Volcano, Hokkaido. *J. Fac. Sci. Hokkaido Univ.*, Ser. IV, **21**, 183–195.

KITAMURA, N., SUGAWARA, Y., SUZUKI, Y., FUJII, K., ITO, O. and TAKAHASHI, S., 1968. Geology of the Miyashita district. Quadrangle series, scale 1/50,000, Fukushima Pref. Government Office, 21 pp. (in Japanese).

KOIDE, H. and BHATTACHARJI, S., 1975. Formation of fractures around magmatic intrusions and their role in ore localization. *Economic Geol.*, **70**, 781–799.

KOMURO, H., KODAMA, K. and FUJITA, Y., 1977. Numerical analysis on the mechanism of the collapse basin formation due to local uplift in the Green Tuff orogenesis. *J. Geol. Soc. Jpn.*, **83**, 277–288 (in Japanese).

————, 1978. The formation of the Late Miocene collapse basin at the Yanaizu district, Fukushima Prefecture, Japan. *Earth Sci.*, **32**, 68–82 (in Japanese).

————, and FUJITA, Y., 1980. Experimental study on the formation of the collapse basin in the Green Tuff orogenesis. *J. Geol. Soc. Jpn.*, **86**, 327–340 (in Japanese).

————, 1984. Uplift and volcanic collapse depression during middle to late Miocene age in the Miyashita district, Aizu, Fukushima Prefecture, Northeast Japan. *J. Geol. Soc. Jpn.*, **90**, 441–454 (in Japanese).

KOUDA, R. and KOIDE, H., 1978. Ring structure, resurgent cauldron and ore deposits in the Hokuroku volcanic field, northern Akita, Japan. *Mining Geol.*, **28**, 233–244.

KOYANAGI, R. Y. and ENDO, E. T., 1976. Seismic activity on the island of Hawaii, 1970 to 1973. *Geophys. Monogr.*, 19, 169–172.

KUBOTA, S. and BERG, E., 1967. Evidence for magma in the Katmai volcanic range. *Bull. Volcanol.*, **31**, 175–214.

LEUDKE, R. G. and BURBANK, W. S., 1966. Volcanism in the western San Juan Mountains, Cololado. *Bull. Volcanol.*, **29**, 345–346.

LIPMAN, P. W., 1976. Caldera-collapse breccias in the western San Juan Mountains, Colorado. *Geol. Soc. Am. Bull.*, **87**, 1397–1410.

MARSH, B. D., 1984. On the mechanics of caldera resurgence. *J. Geophys. Res.*, **89**, 8245–8251.

MASUDA RESEARCH GROUP, 1982. Paleogene Masuda cauldrons. *J. Geol. Soc. Jpn.*, **88**, 321–335 (in Japanese).

MOGI, K., 1978. Relations between the eruptions of various volcanoes and the deformation of the ground surface around them. *Bull. Earthq. Res. Inst. Univ. Tokyo*, **36**, 99–134.

MURAKAMI, N., 1973. A consideration on the mechanism of formation of the Paleogene Tamagawa cauldron. *Mem. Geol. Soc. Jpn.*, 9, 93–105 (in Japanese).

————, IMAOKA, T. and IZUTSU, K., 1982. Geology and structure of Paleogene Haza cauldron, Shimane Prefecture, Southwest Japan. *J. Geol. Soc. Jpn.*, **88**, 311–319 (in Japanese).

NAKAMURA, K., 1969. A hypothesis of island arc tectonics. *Abstracts of the Symposium on Green Tuff Movement*, 31–38. Assoc. Geol. Collab. Jpn. (in Japanese).

New Energy Foundation, 1984. Report of Geothermal Research. No. 8 Aizu district, 811 pp. (in Japanese).

Oide, K., 1968. Geotectonic conditions for the formation of the Krakatau-type calderas in Japan. *Pacific Geol.*, **1**, 119–135.

Olson, P. and Nam, S., 1986. Formation of seafloor swells by mantle plumes. *J. Geophys. Res.*, **91**, 7181–7192.

Otsuka, Y., 1941. On the fauna of the Neogene between Honzyo and Kurosawajiri. *J. Jpn. Assoc. Petrol. Tech.*, **9**, 147–157 (in Japanese).

Parker, T. J. and McDowell, A. N., 1955. Scale models as guide to interpretation of salt-dome faulting. *Bull. Am. Assoc. Pet. Geol.*, **35**, 2076–2086.

Phillips, W. J., 1974. The dynamic emplacement of cone sheets. *Tectonophysics*, **24**, 69–84.

Ramberg, H., 1970. Model studies in relation to intrusion of plutonic bodies. *Geol. J. Spec. Issue*, **2**, 261–286.

Richey, J. E., 1961. British regional geology, Scotland: the Tertiary volcanic districts. Her Majesty's Stationary Office, Edinburgh, 120 pp.

Rittmann, A., 1936. Vulkane und ihre Tätigkeit, Ferdinand Enke Verlag, Stuttgart.

Roberts, J. L., 1970. The intrusion of magma into brittle rocks. in: Newall, G. and Rast, N. (eds.), Mechanism of Igneous Intrusion. *Geol. J. Spec. Issue*, **2**, 287–338.

Robson, G. R. and Barr, K. G., 1964. The effect of stress on faulting and minor intrusions in the vicinity of the magma body. *Bull. Volcanol.*, **27**, 315–330.

Sanders, C. O., 1984. Location and configuration of magma bodies beneath Long Valley, California, determined from anomalous earthquake signals. *J. Geophys. Res.*, **89**, 8287–8302.

Sanford, A. R., 1959. Analytical and experimental study of simple geologic structures. *Geol. Soc. Am. Bull.*, **70**, 19–52.

Sato, H., Otsuki, K. and Amano, K., 1982. Neogene tectonic stress field of Northeast Honshu Arc. *Structural Geol.*, **27**, 55–79 (in Japanese).

——, 1986. Neogene tectonics in central Northeast Japan arc. Abstract of the 40th congress of Assoc. Geol. Collab. Jpn., 146–149 (in Japanese).

Self, S., Goff, F., Gardner, J. N., Wright, J. V. and Kite, W. M., 1986. Explosive rhyolitic volcanism in the Jemes Mountains: Vent locations, caldera development and relation to regional structure. *J. Geophys. Res.*, **91**, 1779–1798.

Shimada, I. and Izawa, T., 1969. Geology of the Tadami district. Quadrangle series, scale 1/50,000, Fukushima Pref. Office, 39 pp. (in Japanese).

—— and Hirabayashi, T., 1972. Geologic structure of the Kuroko Metalliferous province in the western Aizu district, Fukushima Prefecture. *Mining Geol.*, **22**, 329–346 (in Japanese).

—— Neda, T., Kuroe, R. and Izawa, T., 1974. Geology of the Kobayashi district. Quadrangle series, scale 1/50,000, Fukushima Pref. Office, 29 pp. (in Japanese).

—— and Ueda, Y., 1979. K-Ar dating on acidic rocks from the western Aizu district, Fukushima Prefecture. *J. Jpn. Assoc. Min. Pet. Econ. Geol.*, **74**, 387–394 (in Japanese).

Shimamoto, T., 1974. Application of the pi-theorem to the similarity criteria of slow deformation of inhomogeneous viscous fluids. *Tectonophysics*, **22**, 253–263.

Shimazu, M., 1973. On the Tsugawa-Aizu province in the Green Tuff region of the northeastern Japan. *Mem. Geol. Soc. Jpn.*, **9**, 25–38 (in Japanese).

Smith, R. L. and Bailey, R. A., 1968. Resurgent cauldrons. *Geol. Soc. Am. Mem.*, **116**, 613–662.

Steven, T. A. and Ratte, J. C., 1965. Geology and structural control of ore deposition in the Creede district, San Juan Mountains, Colorado. *U.S.G.S. Prof. Paper*, **487**, 90 pp.

Suzuki, K., 1951. The geology of the west region of the Aizu basin, Fukushima Prefecture, part I, central area. *J. Geol. Soc. Jpn.*, **57**, 379–386, 449–456 (in Japanese).

———— and Yᴏsʜɪᴅᴀ, T., 1956.   The Tertiary and Quaternary systems in the south-western part of the Aizu basin, Fukushima Prefecture, a study of the historical geology of the western part of the Aizu basin (II).   *J. Geol. Soc. Jpn.,* **62**, 161–176 (in Japanese).

————, 1964.   Geological map of Fukushima Prefecture, 1/50,000 "Aizu District". Fukushima Pref. Office, 57 pp. (in Japanese).

————, Yᴀsʜɪᴍᴀ, R., Yᴏsʜɪᴅᴀ, T., Nɪsʜɪᴍᴜʀᴀ, S., Mᴀɴᴀʙᴇ, K. and Kᴏʙᴀʏᴀsʜɪ, S., 1968.   Geology of the Nozawa district. Quadrangle series, scale 1/50,000, Fukushima Pref. Office, 61 pp. (in Japanese).

————, Fᴜᴊɪᴛᴀ, Y., Yᴀsʜɪᴍᴀ, R., Yᴏsʜɪᴅᴀ, T., Mᴀɴᴀʙᴇ, K., Hᴀᴋᴏᴢᴀᴋɪ, T., Hᴀɢɪᴡᴀʀᴀ, S., Sʜᴜᴛᴏ, K. and Tsᴜɴᴏᴅᴀ, F., 1972.   Geology of the Wakamatsu district. Quadrangle series, scale 1/50,000, Fukushima Pref. Office, 61 pp. (in Japanese).

————, Mᴀɴᴀʙᴇ, K. and Yᴏsʜɪᴅᴀ, T., 1977a.   The late Cenozoic stratigraphy and geologic development of the Aizu Basin, Fukushima Prefecture.   *Mem. Geol. Soc. Jpn.,* 14, 17–44 (in Japanese).

————, Yᴏsʜɪᴅᴀ, T. and Mᴀɴᴀʙᴇ, K., 1977b.   The geologic development of inland basins in the southern part of the Tohoku District, Japan.   *Mem. Geol. Soc. Jpn.,* 14, 45–64 (in Japanese).

————, Sʜɪᴍᴀᴢᴜ, M., Sʜɪᴍᴀᴅᴀ, I. and Mᴀɴᴀʙᴇ, K., 1986.   Traverse route No. 28 across Japan arc. In: Kɪᴛᴀᴍᴜʀᴀ, N. (ed.), Data Book of Neogene Northeast Japan arc, 3, 28, 15 pp. (in Japanese).

Tᴀᴋᴇᴜᴄʜɪ, A., 1981.   Tertiary stress field and tectonic development of the southern part of the Northeast Honshu Arc, Japan.   *J. Geol. Soc. Jpn.,* **87**, 737–751 (in Japanese).

Wɪʟʟɪᴀᴍs, H., 1941.   Calderas and their origin.   *Bull. Dept. Geol. Sci., Univ. Calif. Publ.,* **25**, 239–346.

———— and McBɪʀɴᴇʏ, A. R., 1979.   Volcanology.   Freeman Cooper, N.Y., 397 pp.

Wɪᴛʜᴊᴀᴄᴋ, M. O. and Sᴄʜᴇɪɴᴇʀ, C., 1982.   Fault patterns associated with domes—experimental and analytical study.   *Bull. Am. Assoc. Pet. Geol.,* **66**, 302–316.

Yᴀᴍᴀᴅᴀ, Y., 1980.   Plasticity and Visco-elasticity.   Baifu-kan, Tokyo, 262 pp. (in Japanese).

Yᴏᴋᴏʏᴀᴍᴀ, I., 1958.   Review of geophysical researches on Volcano O-sima.   *Bull. Volcanol. Soc. Jpn.,* ser. 2, **3**, 39–69.

————, 1963.   Volcanic calderas and meteorite craters with the special relation to their gravity anomalies.   *J. Fac. Sci., Hokkaido Univ.,* ser. VII, **2**, 37–47.

————, 1969.   Some remaeks on calderas.   *Bull. Volcanol. Soc. Jpn.,* ser. 2, **14**, 77–83.

————, 1974.   Calderas and their formation.   *Monogr. Assoc. Geol. Collab. Jpn.,* 18, 41–53 (in Japanese).

Yᴏsʜɪᴅᴀ, T., 1984.   Tertiary Ishizuchi cauldron, southwestern Japan arc: formation by ring fracture subsidence.   *J. Geophys. Res.,* **89**, 8502–8510.

Yᴏsʜɪᴛᴀɴɪ, A. and Yᴀᴍᴀᴜᴄʜɪ, S., 1981.   Fracture systems distributed in the basement of Green-Tuff sedimentary basin in the earliest stage of basin formation.   *Report of Fac. Education, Tottori Univ., Natural Sci.,* **30**, 89–95 (in Japanese).
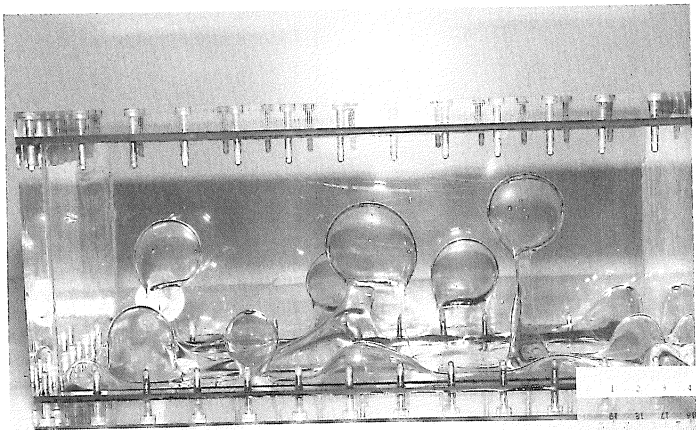
Explanation of Plate I

Fig. 1.   Sedimentary breccia at the margin of the Honna Formation.

Fig. 2.   Vertical fault in the basement near the margin of the Honna Formation.
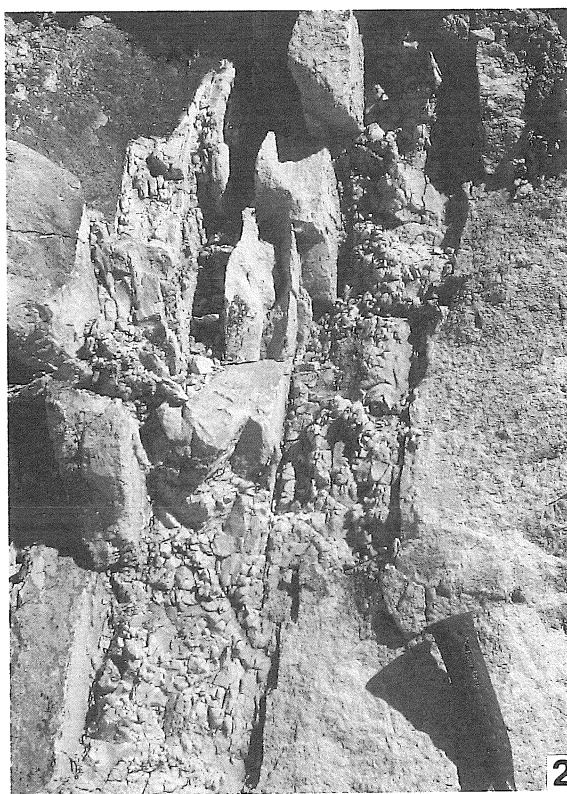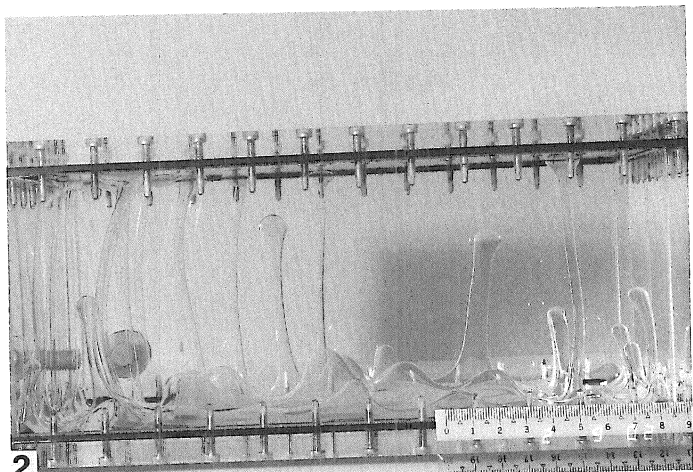
Explanation of Plate II

Fig. 1. Model experiment on diapir evolution (1). A tight rectangular acrylic-glass box (10×15×25 cm) was filled completely with the source buoyant layer of silicone oil and the overburden layer of syrop. Buoyant layer: 0.6 cm in thickness, 0.98 g/cm^3 in density, and 1.1×10^2 Pas in viscosity. Overburden layer: 9.4 cm in thickness, 1.49 g/cm^3 in density, and 3.0×10^3 Pas in viscosity. This photo was taken after 37 minutes from the start. (scale in cm)

Fig. 2. Model experiment on diapir evolution (2). Buoyant layer: 0.5 cm in thickness, 0.98 g/cm^3 in density, and 1.1×10^2 Pas in viscosity. Overburden layer: 9.5 cm in thickness, 1.36 g/cm^3 in density, and 9.75 Pas in viscosity. This photo was taken after 7 minutes from the start. (scale in cm)

Fig. 3. Model S–5. Collapse structure formed by subsurface cavity.
Collapse structure produced ca. 30 minutes later from the beginning of the test. Vertical photograph of the model.

Fig. 4. Model S–5. Oblique photograph.
Note ring fractures and the collapse wall dipping outward.

PLATE II